

## Article

# Shadow-Based Hierarchical Matching for the Automatic Registration of Airborne LiDAR Data and Space Imagery

Alireza Safdarinezhad, Mehdi Mokhtarzade \* and Mohammad Javad Valadan Zoej

Faculty of Geodesy and Geomatics, K. N. Toosi University of Technology, Tehran 19667-15433, Iran; safdari\_nezhad@sina.kntu.ac.ir (A.S.); valadanjouj@kntu.ac.ir (M.J.V.Z.)

\* Correspondence: m\_mokhtarzade@kntu.ac.ir; Tel.: +98-218-877-0218

Academic Editors: Guoqing Zhou and Prasad S. Thenkabail

Received: 26 March 2016; Accepted: 25 May 2016; Published: 3 June 2016

**Abstract:** The automatic registration of LiDAR data and optical images, which are heterogeneous data sources, has been a major research challenge in recent years. In this paper, a novel hierarchical method is proposed in which the least amount of interaction of a skilled operator is required. Thereby, two shadow extraction schemes, one from LiDAR and the other from high-resolution satellite images, were used, and the obtained 2D shadow maps were then considered as prospective matching entities. Taken as the base, the reconstructed LiDAR shadows were transformed to image shadows using a four-step hierarchical method starting from a coarse 2D registration model and leading to a fine 3D registration model. In the first step, a general matching was performed in the frequency domain that yielded a rough 2D similarity model that related the LiDAR and image shadow masks. This model was further improved by modeling and compensating for the local geometric distortions that existed between the two heterogeneous data sources. In the third step, shadow masks, which were organized as segmented matched patches, were the subjects of a coinciding procedure that resulted in a coarse 3D registration model. In the last hierarchical step, that model was ultimately reinforced via a precise matching between the LiDAR and image edges. The evaluation results, which were conducted on six datasets and from different relative and absolute aspects, demonstrated the efficiency of the proposed method, which had a very promising accuracy on the order of one pixel.

**Keywords:** 3D registrations; shadows; LiDAR; HRSI (High Resolution Satellite Imagery); automatic matching

## 1. Introduction

At this time, with the advent of various remote sensing sensors (e.g., optical, thermal, RADAR, and LiDAR), multisource data exploitations are considered to be the most effective techniques. Thereby, data registration, which is a prerequisite for all multisource techniques, arises as a major research topic, especially when one looks for a reliable and accurate automatic method.

In its common structure for most remote sensing applications, data registration consists of successive steps that include feature extraction, feature correspondence, transformation model determination and resampling [1]. Among those steps, the first and second ones, which lead to control features for the solution of a transformation model, are the most challenging, particularly when dealing with the registration of heterogeneous data sources (e.g., LiDAR-optic, RADAR-optic, and LiDAR-RADAR).

This paper aims to design an automatic registration method between LiDAR data and High Resolution Satellite Images (HRSI). LiDAR data and HRSI, as examples of heterogeneous data sources, are unlike in different aspects: 1—the nature of the data acquisition (*i.e.*, irregular 3D points cloud

*vs.* rasterized imaging), 2—representation geometry (orthogonal projection *vs.* perspective geometry of images), and 3—radiometric content (height in LiDAR *vs.* reflected electromagnetic radiation in images).

Common registration techniques are mainly designed or developed for same sensor registration and are rarely applicable for LiDAR and optical data source matching. This is mainly due to the different information content of LiDAR data and pictorial images, as reported in [2–8].

In this paper, as the main contribution, shadows were considered to serve as the identical nature-matching candidates. For this reason, shadow extraction techniques, which were individually developed for each data source, were implemented, leading to reliable matching entities with high generalization ability. The obtained shadow masks were then used in a hierarchical matching procedure, which yielded a dense set of corresponding points between the 3D LiDAR data and 2D HRSI pixels. These control points were ultimately used to determine a fine 3D registration model, which in this case was a 3D affine one.

The existing methods are reviewed to first justify the motivation of the current research. Section 3 is devoted to an introduction of the applied input data sets, and in Section 4, the details of the proposed hierarchical method are explained accompanied by step-by-step implementation results. The evaluation and discussion of the results are presented in Section 5, and the paper ends with the concluding points and suggestions in Section 6.

## 2. Motivations and Related Works

As a prerequisite for the integrated exploitation of LiDAR data and optical satellite/aerial images, their registration is commonly addressed via a 3D model that transforms the ground coordinates of LiDAR points to their relevant positions in the image space [9,10].

To solve those models, common points are usually identified and extracted manually from both data sources to serve as control points. However, this manual task is tedious and prone to mistakes because 1—the information content in the LiDAR data and images are different (*i.e.*, it is difficult to compare them visually), 2—in LiDAR data taken from dense urban areas, it is difficult to identify individual 3D features as the matching candidate, and 3—regarding the sampling interval in LiDAR data, it is not guaranteed to locate a 3D point at the corner of objects, which is the most appropriate position to make a match candidate [1].

In addition to relieving the above-mentioned problems, automatic methods can address the high rate of data acquisition of recent years. Accordingly, there is much motivation to design and develop reliable automatic methods that deal with the registration of LiDAR data to aerial/satellite images. Matching problems between LiDAR and optical images have been the subject of various researches, some of the most recent of which will now be briefly discussed.

In the area-based matching technique proposed in [11], the radiometric content of the grid-based LiDAR and optical images was equalized via a linear transformation. The underlying assumption (*i.e.*, the existence of a linear radiometric model between inherently different grids based LiDAR data and optical images) could not be generalized.

In two other area-based matching techniques in [3,4], mutual information (MI) was applied as a radiometric similarity measure. In those methods, the height and intensity information of the LiDAR data were applied to strengthen the results. They both concluded that MI outperforms other similarity measures. However, those methods are highly dependent on LiDAR intensity information, which narrows their applicability, especially when only the height information layers (e.g., available DSMs) are used.

A novel area-based technique was presented in [10] in which intensity data of LiDAR was used to compensate for the existing bias between LiDAR and orthogonal optical images. In that paper maximum correlation was applied as the similarity criterion which could be a good measure since both data sources were in the same ground coordinate system, there were negligible differences between data sets and also vertical displacement have been already removed in the orthogonal optical image.

In addition to the above-mentioned area-based methods, feature-based techniques are also applied to address the registration of LiDAR data to pictorial images. For this reason, common to all feature-based methods, salient features are first extracted from both data sources that are then matched together according to their description vectors. These steps are usually undertaken in a hierarchical procedure to increase the reliability of the results. The methods reported in [6–8] are all instances of feature-based techniques applied to match LiDAR data and optical images. High numbers of miss-matched features as well as non-proportioned numbers of features extracted from optical images and LiDAR data are common problems of feature-based methods.

LiDAR intensity was used in [5], where the well-known SIFT method was applied to register it to optical images. They faced an unbalanced number of features in the two data sets and a large number of blunders. To address those restrictions, the Baarda statistical test and RANSAC algorithm were applied.

Extracted building masks were also used in [2,12] to address the geometric registration of LiDAR and aerial images. In those building-based methods, flat building roofs, which are subject to failure in dense urban areas, were extracted for isolated and well-structured buildings via naive methodologies. However, those methods are not applicable to rural regions where no buildings are available.

Most of the reviewed methods, irrespective of being area-based or feature-based, are highly affected by the intensity information in LiDAR data, which reduces their generality and also makes them inapplicable to DSMs. To develop a more reliable method applicable to all height information, we looked for features with identical natures in both height and optical data. In this survey, shadows, which frequently occur in both urban and rural areas, were chosen. The shadows were reconstructed from LiDAR data and also detected in HRSI. The two shadow sets, which were expected to have the same geometrical structure, were applied to the matching.

Shadows refer to that part of the environment where direct sunlight is obstructed by ground features. The visual perception of the spatial topology of features and phenomena facilitates identifying and following shadows. From a human perspective, shadows are a significant proportion of the features in satellite images that can be used to facilitate the visual interpretation of three-dimensional features in the image.

Shadow detection is a prerequisite of many remote sensing applications. In most interpretation tasks, shadows are regarded as interfering features that should be masked or at least reduced to better identify other features of interest [13–18]. On the other hand, shadows are sometimes detected as geometrical interpretive features. Detected shadows with sun-azimuth and sun-elevation data can lead to information on the height of their corresponding features [19–22].

The main motivations for utilizing shadows as common features for LiDAR data and HRSI registration are as follows.

- Shadows are among the high contrast features in optical images and are thus very prone to be successfully detected. In addition, there is a rich research background on their detection strategies, which are mainly much more simplistic in comparison to those of other features such as buildings.
- Shadows are very common and are usually evenly distributed in urban and rural areas. This is a very appealing characteristic for a candidate feature in matching techniques.
- Shadows can be reconstructed easily from height information with very simple geometric analyses. This techniques do not require LiDAR intensity information, which makes them applicable to either LiDAR data or other height information layers (e.g., DSMs).

### 3. Dataset and Pre-Processing

Six different regions in San Francisco were used as the input dataset; each was comprised of a QuickBird (QB) sub-image and corresponding aerial LiDAR data. There was a three-year interval between the optical images and LiDAR data that resulted in some changed regions, especially in urban areas. The six applied datasets, which are shown in Figure 1 and specified in Table 1, were selected to cover different textures, urban densities and local topographies.





**Figure 1.** The area covered by the LiDAR data and the QB image in the applied data set. Control points in each dataset are shown via yellow marks.

**Table 1.** Specifications of the applied data sets.

Dataset	Panchromatic Area (Km <sup>2</sup> )	LiDAR Area (Km <sup>2</sup> )	Elevation Range (m)	Overlap %	Control Points	3D-Model RMSE (Pixels)
1 (Sample)	2.25	2.16	88.4	95.8	84	0.72
2	2.25	2.12	55.6	94.3	21	0.85
3	2.25	2.17	114.1	96.7	19	0.94
4	2.25	2.24	119.5	99.7	25	1.07
5	2.18	1.92	118.8	87.8	16	0.73
6	1.08	1.08	57.8	100	15	0.75

Figure 2 shows some instances of the changes occurred during the time difference between LiDAR data and satellite image acquisitions.

The QB image was taken on 11 November 2007 with 170.7° and 34.4° sun azimuth and elevation respectively. The image is comprised of a 0.6 m panchromatic and four 2.4 m spectral bands. The pan-sharpening process of this image was implemented using the Gram-Schmidt algorithm in ENVI 4.8. It outperforms most other pan-sharpen methods in both maximizing image sharpness and minimizing color distortion. It is, on the other hand, also more complex and computationally expensive than most other methods, as it requires forward and backward transforming the entire image [23].

The aerial LiDAR data related to the same spatial domain were obtained by an Optech ALTM3100EA system from 11 flight missions in 2010. The data were collected using a maximum of four returns at a nominal resolution of 2 to 3 points per square meter. To convert the irregular point cloud to a raster grid, the covered regions of the LiDAR data were rasterized into a 0.4 m × 0.4 m



regular grid. The irregular points in each grid cell were identified, and the height of the highest point was assigned to that cell. Finally, a median filter with a  $5 \times 5$  kernel size was implemented to remove noisy regions.

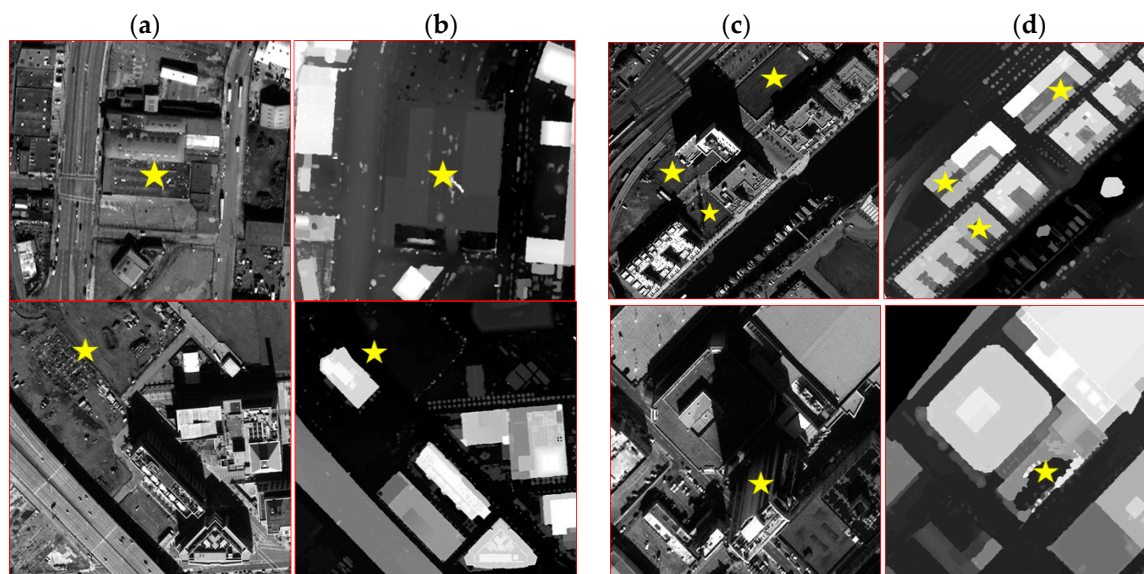


**Figure 2.** (a–d) Some of the salient urban changes occur between the time of QB and LiDAR data acquisition: Columns of (a,c) are QB panchromatic images and columns of (b,d) are corresponding LiDAR data. Changed regions are marked with the yellow stars.

In each dataset, a series of corresponding points was manually extracted from the QB image and LiDAR data for later use in the evaluation of the results. These control points were generally selected in distinct corners for more reliable positioning. An attempt was made to select points well-distributed through the region. The number of control points in each dataset is reported in the last column of Table 1.

Dataset number 1 was selected as the sample (Figure 3). In addition to more detailed quantitative evaluations, the step-by-step results for that dataset are presented and discussed. A higher number of control points were thereby gathered, allowing the opportunity to develop a fine reference 3D model (*i.e.*, essential for absolute and relative result evaluations).

A 3D affine model ( $M$ ) was used to relate the 3D coordinates of the LiDAR points in the ground coordinate system ( $X, Y, Z$ ) to their relevant 2D digital positions ( $r, c$ ) in the HRSI space (Equation (1)).

$$[r, c]^T = [M] \times [X, Y, Z, 1]^T, M = \begin{bmatrix} m_1 & m_2 & m_3 & m_4 \\ m_5 & m_6 & m_7 & m_8 \end{bmatrix} \quad (1)$$

This model not only benefits from an appealing simplicity but also fits sufficiently well to the HRSI due to their small fields-of-view [24]. In addition, most modern satellite images are initially corrected for primary geometrical errors, which justify the use of a simple 3D affine as their relating models. The 3D affine model, when solved using the manually extracted control points, was designated as the control model ( $M^{Ctrl}$ ) and subsequently applied to the evaluation of the results.

In Figure 2a, the error vectors (*i.e.*, the displacement vectors between the computed image coordinate of the control model and their true image positions) are superimposed on the QB image and shown in red. A quantitative accuracy assessment of the control model was also performed using independent check points (*i.e.*, control points that were not applied in the solution of the 3D affine model), as reported in the last column of Table 1.

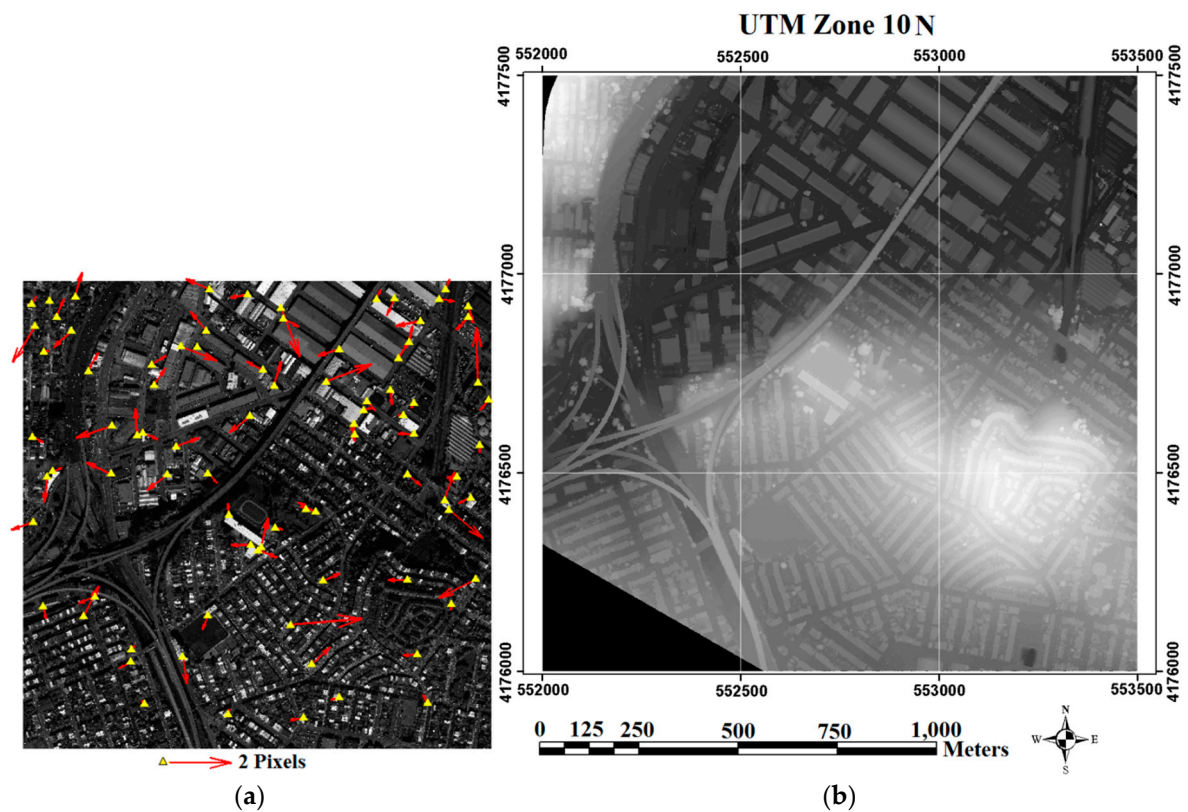


**Figure 3.** A view of the sample dataset: (a) QB panchromatic image from the sample dataset; (b) Raster LiDAR data from the sample dataset.

#### 4. Methodology and Results

The underlying concept of the proposed method is that shadows were considered as common extractable features in the LiDAR data and HRSI and were thus used as the candidate matching entities. Therefore, it can be categorized into feature-based registration techniques. Accordingly, LiDAR and HRSI shadow masks were first extracted. The masks were subsequently registered using a four-step hierarchical strategy in which the registration was improved successively. Figure 4 shows a diagram of the proposed method.

As shown in the above figure, the LiDAR and HRSI shadow masks were first roughly registered in their 2D digital coordinate systems (rows and columns), which led to a coarse 2D model. To do so, both shadow masks were transformed to the frequency domain, where the parameters of a 2D conformal transformation model (*i.e.*, scale, rotation and two translations) were determined (Section 4.2). Second, local distortions from the different LiDAR and HRSI geometries were modeled to strengthen the coarse 2D model (Section 4.3). Third, the shadow masks were segmented and matched together, which produced a coarse 3D model (Section 4.3). Finally, the edge information in both data sources was exploited using Iterative Closest Edge Points Matching (ICEPM), and a fine 3D model was estimated as the ultimate registration product (Section 4.4).

The main contributions of the proposed method can be summarized as the use of shadows as matching entities between LiDAR and HRSI and fully automatic registration schemes, which did not require initial information (*i.e.*, an initial relating model between the LiDAR and HRSIs).

The details of the proposed method are presented in the following section.

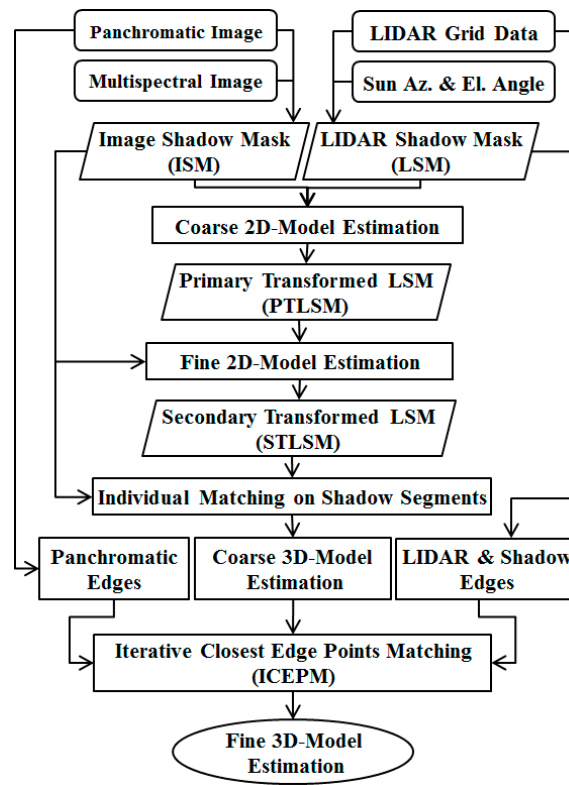


**Figure 4.** A diagram of the proposed automatic registration of the LiDAR and HRSI.

#### 4.1. Automatic Shadow Extraction

##### 4.1.1. Automatic Shadow Extraction in HRSI

To date, several algorithms have been developed for shadow detection and segmentation from remote sensing images [25,26]. These methods have very diverse methodologies such as texture and morphology features [15,16], enhancing and thresholds [14], color spaces and spectral characteristics [15,17,18,26–31], region growing segmentation [15], using complementary data such as DSM [13] and hybrid strategies [14,15]. It is worth noting that the radiometric similarity of shadows and features with low reflectance (e.g., water, asphalt, etc.) is one of the main challenges in this field.

In most HRSI, spectral bands are available along with the panchromatic images. Therefore, it is preferable to exploit all of these bands for shadow detection. Accordingly, the proposed shadow detection algorithm was designed in the spectral feature space, where it was intended to be fully automatic (*i.e.*, needed no operator interaction) [32].

Among the variety of proposed spectral features for shadow detection, two groups that are based on the color invariant transforms were used in this study [29–31]. These features are introduced in Equations (2)–(8).

$$C_1 = \arctan\left(\frac{B}{\arg \max \{G, R, NIR\}}\right) \quad (2)$$

$$C_2 = \arctan\left(\frac{G}{\arg \max \{R, B, NIR\}}\right) \quad (3)$$

$$C_3 = \arctan\left(\frac{R}{\arg \max \{B, G, NIR\}}\right) \quad (4)$$

$$C_4 = \arctan\left(\frac{NIR}{\arg \max \{R, G, B\}}\right) \quad (5)$$



$$C_5 = \log\left(\frac{B}{G}\right) \quad (6)$$

$$C_6 = \log\left(\frac{R}{G}\right) \quad (7)$$

$$C_7 = \log\left(\frac{NIR}{G}\right) \quad (8)$$

In the above equations, B, G, R and NIR are blue, green, red and near infrared bands respectively. Equations (5) and (8) were not proposed in the original references [29–31] but were extended in this study due to the availability of the NIR band and its effectiveness in vegetation suppression.

These features, when normalized, were used to discriminate shadows from non-shadow regions. Figure 5 shows these normalized features beside the panchromatic image for a subset of QB image. They are specifically designed to provide separation of shadows from other image features [29–31]. Visual inspection of Figure 5 demonstrates the separability of the shadows by these features.

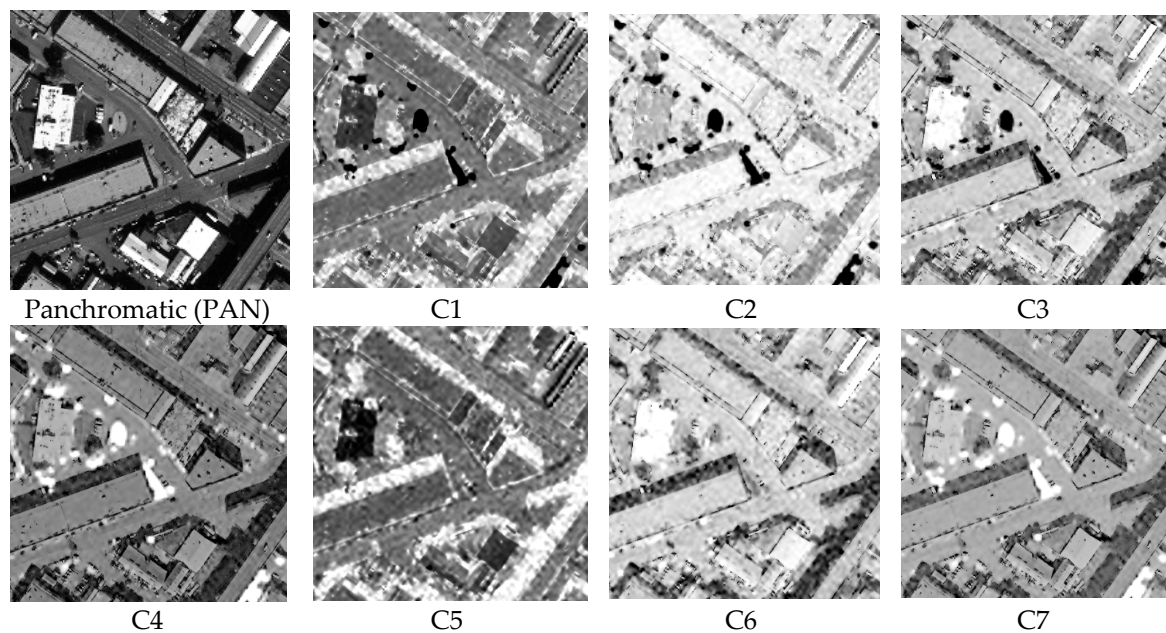


**Figure 5.** Normalized panchromatic and color invariant features (Equations (2)–(8)) used for shadow extraction.

The above mentioned features, called Normalized Color Invariant Features (NCIFs), were then applied in traditional K-Means clustering to recognize pixels in the shadow regions. The preliminary image clustering results via the NCIFs showed promising separability of shadow with other phenomena. In this respect, shadow cluster was characterized as a resistant cluster against the variations in the number of clusters. Figure 6 shows the K-Means clustering results for different cluster numbers. In this figure, shadow cluster is shown by red.

For designing a fully automatic process, clustering initialization, setting parameters and the automatic recognition of shadow cluster are the main challenges to be addressed. A novel clustering strategy, incremental clustering, was therefore designed and is described below [32].

Incremental clustering was conceptually designed based on a geometric and a radiometric interpretation of shadow characteristics. In the geometric interpretation of shadows, their separability with other phenomena was considered. In that respect, a shadow cluster was characterized as a resistant cluster against the variations in the number of clusters. In other words, it was expected that the cluster containing shadow pixel would have negligible changes when the clustering was repeated

with different number of initial clusters. This characteristic was quantified via a Geometric Index (GI), which is described later.

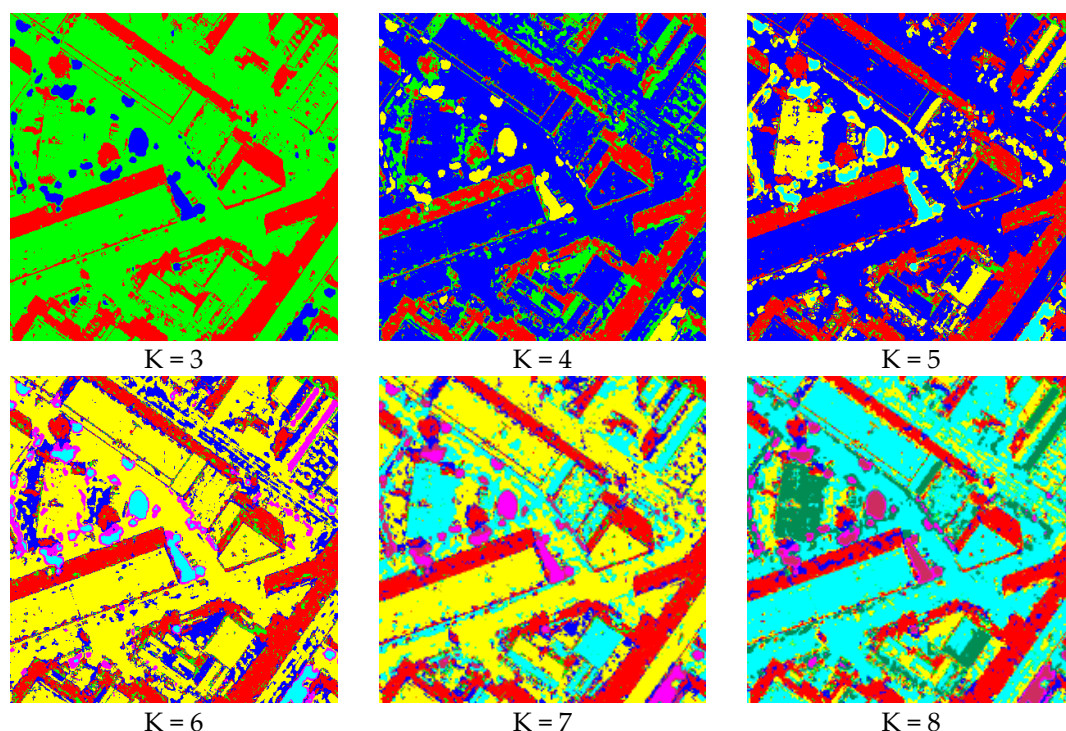


**Figure 6.** K-Means clustering results in the NCIFs feature space. Shadow cluster is shown by red.

In the radiometric interpretation of shadows, their homogenous and dark natures were considered. Accordingly, the shadow cluster was characterized as a cluster that contained pixels with low intensities (*i.e.*, digital numbers, DNs) in the panchromatic image. This radiometric interpretation was also quantified via a Radiometric Index (RI), which is introduced later.

According to these two interpretations, an iterative and fully automatic shadow extraction process was designed and is described in the next page entitled as Algorithm 1.

According to the Algorithm 1, a binary mask, NI, is produced in each iteration, which is finally (*i.e.*, after the convergence of iterations) regarded as the initial Image Shadow Mask (iISM). The iteration is repeated until NI experienced less than a 3% change in two successive iterations.

In this algorithm, clustering maps ( $cm^j$ ;  $j = 1, 2, \dots, n$ ) are produced through a gradual increase in the number of clusters ( $K_j$ ). A majority filter is then applied to each cluster map to improve its spatial consistency.

In line 12 and in each iteration, all possible clusters permutations (*i.e.*,  $\{CP\} = \{CP_1, CP_2, \dots, CP_{m_n}\}$ ) are generated. Each permutation is comprised of an  $n$ -member set of  $C_i^j$  binary maps. Each binary map, say  $C_i^j$ , is related to one of the clusters (according to the permutation order) in the  $j^{\text{th}}$  clustering map,  $CM^j$  (Equation (9)).

$$CP_i = \{C_i^1, C_i^2, \dots, C_i^{m_n}\}, i = 1, 2, \dots, m_n \quad (9)$$

Given that  $cm^1, cm^2, \dots, cm^n$  consists of  $K_1, K_1 + 1, \dots, K_n$  clusters, respectively, the number of all possible permutations,  $m_n$ , is shown in Equation (10).

$$m_n = K_1 \times (K_1 + 1) \times (K_1 + 2) \times \dots \times K_n = K_n! / (K_1 - 1)! \quad (10)$$

A map intersection ( $MI_i$ ) was produced from each permutations of  $\{CP_i\}$  as shown in Equation (11).

$$MI_i = \left\{ C_i^1 \cap C_i^2 \dots \cap C_i^n \right\} = \bigcap_{j=1}^n C_i^j \quad i = 1, 2, \dots, m_n \quad (11)$$

The Shadow Fitness of each map intersection  $MI_i$  is computed according to its geometric and radiometric indices, as shown in Equation (12).

$$SF_i = \frac{GI_i}{RI_i}, \quad i = 1, 2, \dots, m_n \quad (12)$$

The Geometric and Radiometric Indices, which are represented by  $GI_i$  and  $RI_i$ , respectively, are computed for each map intersection  $MI_i$  using Equations (13) and (14).

$$GI_i = \frac{n \times \text{Nr}(MI_i)}{\sum_{j=1}^n \text{Nr}(C_i^j)} \quad (13)$$

$$RI_i = \text{mean}(\text{PAN} \langle MI_i \rangle) + \text{std}(\text{PAN} \langle MI_i \rangle) \quad (14)$$

Here,  $\text{Nr}()$  is a counter of the number of pixels with true values in a binary image, and  $\text{PAN} \langle MI_i \rangle$  represents a vector of normalized PAN digital numbers taken from the pixels assigned to  $MI_i$ .

---

**Algorithm 1** Incremental Clustering for Shadows Detection

---

Input: Normalized Panchromatic Image (PAN)  
 Normalized Color Invariant Features (NCIFs)  
 Output: Image Shadow Mask

---

```

1   $n = 1$  /* Iteration Number /
2   $K_n = 3$  /* minimum number of clusters /
3   $cm^1 \leftarrow K_1$ -Means Clustering of the NCIFs
4  Estimate Radiometric Index (RI) for each  $cm^1$ 's Cluster
5  NI  $\leftarrow$  Set the binary map correspond to the cluster with minimum RI as the New
   Index /* first New Index /
6  BEGIN
7  | LI  $\leftarrow$  Set the NI as the Last Index
8  |  $n \leftarrow n + 1$ 
9  |  $K_n \leftarrow K_{n-1} + 1$ 
10 |  $cm^n \leftarrow K_n$ -Means Clustering of the NCIFs
11 | Majority filtering of the  $cm^n$  /* to improve its spatial consistency /
12 |  $\{CP\} \leftarrow$  Generate all Clusters Permutations among  $\{CM\} = \{cm^1, \dots, cm^n\}$ 
13 |  $\{MI\} \leftarrow$  Generate the Map of Intersection for each member of  $\{CP\}$  (Equation (11))
14 |  $\{SF\} \leftarrow$  Estimate Shadow Fitness for each member of  $\{MI\}$  (Equations (12)–(14))
15 | NI  $\leftarrow$  Set the MI correspond the maximum value of SF as the New Index
16 |  $\Theta \in [0, 1] \leftarrow$  Compute the Area Consistency of NI and LI (Equation (15))
17 DO UNTIL  $\Theta < 0.97$ 
18 iISM  $\leftarrow$  Set the NI as the initial Image Shadow Mask
19  $(\mu, \sigma) \leftarrow$  mean and std of  $\text{PAN} \langle iISM \rangle$  after successive blunder removals
20 PAN_Slice  $\leftarrow$  Generate the binary PAN_Slice via (Equation (16))
21 Segment PAN_Slice via N-8 neighborhood analysis
22 FOR all PAN_Slice's segments
23 |  $\text{PAN\_Slice}_i \leftarrow i^{\text{th}}$  PAN_Slice's segment
24 | IF  $(\text{PAN\_Slice}_i \cap iISM) \neq \emptyset$  THEN  $iISM = iISM \cup \text{PAN\_Slice}_i$ 
25 END
26 ISM  $\leftarrow$  Set the iISM as the Image Shadow Mask

```

---



According to Equation (13),  $GI_i$  shows the spatial consistency among the binary maps of a cluster permutation (i.e.,  $\{CP_i\}$ ). If the binary maps associated to  $\{CP_i\}$  (i.e.,  $C^j_i$ ) are similar, then their map intersection  $MI_i$  will be approximately the same as the  $C^j_i$  binary maps, which increases the  $GI_i$  measure for that cluster permutation. In other words, a large value of  $GI_i \in [0, 1]$  indicates an increased stability of the associated clusters in  $\{CP_i\}$  against the increase in the number of clusters. As mentioned before, this index is expected to have large values for a shadow cluster due to its considerable separability with other image phenomena.

Conversely, in Equation (14),  $RI_i$  is an index of the mean and variation of the intensity for the pixels associated with  $MI_i$ . The lower values of  $RI_i$  are expected when all of the clusters are associated to  $\{CP_i\}$ , and thus their map intersection  $MI_i$  belong to dark and homogenous objects such as shadows.

The map intersection  $MI_i$  with the highest SF value is selected as the New Index (NI) map (Line 15). The area consistency of this NI with the Last Index (LI) is then measured via Equation (15) and is used as the convergence criterion. In this equation and in rest of the paper,  $Nr()$  has the same meaning as in Equation (13).

$$\Theta = \frac{2 \times Nr(LI \cap NI)}{Nr(LI) + Nr(NI)} \quad (15)$$

The last NI, which is obtained after the convergence, is considered as the initial Image Shadow Mask (iISM). This iISM, which is the intersection of all of the shadow clusters, suffers from gaps and discontinuity and is thus refined via the panchromatic image (Lines 18–25). To do so, the mean ( $\mu$ ) and standard deviation ( $\sigma$ ) of  $PAN \langle iISM \rangle$  is computed and refined iteratively with a  $2.5\sigma$  statistical test. The  $PAN \langle \rangle$  operator is the same as that in Equation (14). A  $PAN\_Slice$  binary map is then produced via Equation (16).

$$PAN\_Slice(i, j) = \begin{cases} 1 & \text{if } \mu - \sigma < PAN((i, j)) < \mu + \sigma \\ 0 & \text{otherwise} \end{cases} \quad (16)$$

In the above equation,  $PAN(i, j)$  represents the normalized digital number of the panchromatic image in the  $(i, j)$  position. The  $PAN\_Slice$  is then segmented via an N-8 connectivity analysis in which two true-valued pixels are connected when located in the 8 neighboring of each other. Those segments connected to the iISM are finally added to it for gap removal. Figure 7 shows the result of the ISM generation from the sample dataset's QB image.



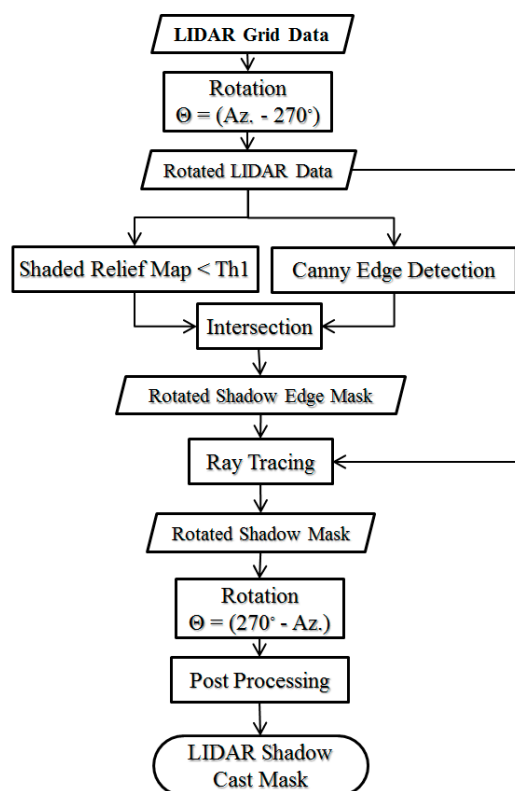
**Figure 7.** The ISM extracted from the sample dataset's QB image: (a) Result of the overall application (White regions are shadows); (b) Enlarging the result of applying algorithm on three regions along the panchromatic image.

Figure 7 shows the success of the proposed ISM extraction in recognizing the shadow cluster. In general, the extracted ISM and true image shadows are similar; however, there are discontinuities in the results as well as some unrecognized shadow pixels.

In order to evaluate the produced ISM, some reference shadow and non-shadow regions were manually identified to form the confusion matrix. Non-shadow regions were mainly selected from dark image objects which are more prone to be misclassified as shadow. The overall accuracy of 91% was achieved while user accuracy of shadow and non-shadow classes were 99% and 82% respectively. Although shadow detection is not the ultimate purpose of this study, the preliminary results are sufficiently satisfactory to motivate the further development of this idea in future research that will concentrate on shadow detection. The separability of shadows from other image objects is an assumption of this method that can be weakened, for example, by high sun elevation angles, the high presence of dark objects (e.g., asphalt) and vast water covered regions. Furthermore, the presence of clouds may degrade the results. These concerns can be the subject of further studies.

#### 4.1.2. Automatic Shadow Extraction in LiDAR

From the geometrical point of view, the LiDAR Grid data (Figure 3b) and relevant information of the light source provide the necessary information for virtual shadow reconstruction. From an assumption of the availability of the sun azimuth (Az.) and elevation angles (Elv.), a simple algorithm was designed for the reconstruction of shadows from LiDAR data. Figure 8 shows a flowchart of the proposed algorithm [32].



**Figure 8.** Flowchart of the shadow reconstruction from raster LiDAR data.

With regard to the assumption of parallel sunlight, the casted shadow will be formed along the inverse sun azimuth. Accordingly, in the first step, the LiDAR data were rotated by  $\theta = \text{Az.} - 270^\circ$ . From the rotation, the layout of the rows in the raster LiDAR data (from left to right) will be in the direction of the inverse sun azimuth. In this situation, the identification of the shadow regions is reduced to a 1D independent search in each row of the rotated raster LiDAR data.

The shadow detection from the rotated raster LiDAR was performed in two main stages: 1—shadow edge detection, which is followed by 2—shadow region detection. The elevated points that caused the shadow regions were found in the first step. These points were then used to find their resultant shadow lines in their relevant row of the LiDAR raster data. In the following, the two steps are described.

### • LiDAR shadow edge detection

Herein, shadow edges are regarded as locally elevated positions where shadow regions originate. Because these edges are locally evaluated, edge detection on the LiDAR raster can be used to find their initial positions. For this, the Canny edge detector is proposed [33].

Although shadow edges are among the Canny results, the inverse is not essentially true. In other words, all of the edge pixels detected by Canny are not necessarily the requested shadow edges. Therefore, a shaded relief mask was designed to exclude non-shadow edge pixels. This process is explained in the following.

In conventional shaded relief analysis, the angle between the surface normal and the sun direction vectors (say  $\alpha$ ) is first determined. The shaded pixels are then marked as those with  $\alpha > \text{threshold}$ . From a theoretical point of view, the threshold should be  $90^\circ$ ; however, higher values can be used to yield more reliable results.

In this step, a shaded relief analysis is performed on all of the edges detected by Canny. Those pixels with  $\alpha < 115^\circ$  are excluded. The obtained binary image is considered to be the shadow edge pixels, which are exploited in the next section.

### • Shadow region detection

In this section, the extracted shadow edges are regarded as the barriers to detect the pixels in their shadows. For that reason, a ray tracing process was implemented. Figure 9 shows the concept applied in this step. In this figure,  $L_{i,j}$  is the rotated position of LiDAR shadows. For all  $j' > j$  the value of Equation (17) is computed in which  $\Delta l$  and  $\Delta h$  represent the horizontal and vertical distances between  $L_{i,j}$  and  $L_{i,j'}$  respectively.

$$\beta = \tan^{-1} \left( \frac{\Delta l}{\Delta h} \right) \quad (17)$$

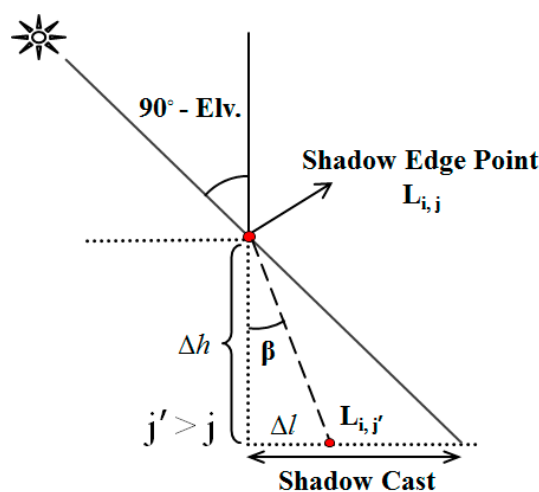


Figure 9. The concept applied for ray tracing process.

Pixels with  $(\beta < 90^\circ - \text{Elv.})$  are considered to be located in the shadow cast. Figure 9 shows the concept applied in this step.

The following pseudocode (Algorithm 2) shows the methodology implemented to detect shadow regions:

In line 5, only the pixels in the same row of the shadow edge pixels are examined due to previous  $\theta = \text{Az.} - 270^\circ$  rotation. This rotation is compensated for in line 11. Angle  $\beta$  in line 7 is computed using the 3D coordinates of the shadow edge pixel and the pixel under investigation. The shadow segment widths, which are applied in line 16, are considered to be the smallest eigenvalues of the covariance matrix of that segment.

The small shadow segment removal at line 17 is justifiable due to factors such as (1) the low probability of the identification of small shadows in the optical images and (2) the noisy nature of the small shadows (e.g., the noise in LiDAR systems and small features such as cars and plants). The *WidthTh* threshold also prevents the formation of tall 3D-features that do not have significant thicknesses (noise and features such as lighting poles). In this paper, those thresholds were set to 100 and 10 pixels for *AreaTh* and *WidthTh*, respectively. The results of the LiDAR shadow extraction on the sample dataset are presented in Figure 10.



**Algorithm 2** Shadow Extraction in LiDARInput: Rotated LiDAR Grid Data ( $\theta = \text{Az.} - 270^\circ$ )

Shadow Edge Pixels

Sun Azimuth and Elevation Angle

WidthTh &amp; AreaTh

Output: LSM

---

```

1 BEGIN /* shadow region detection /
2 | For all shadow edge pixels ( $L_{i,j}$ ) /* found previously /
3 | BEGIN /* shadow line detection /
4 | . In a  $3 \times 3$  window, assign the max elevation to shadow edge pixel
5 | . For  $\{L_{i,j'} \mid j' > j\}$  until the next shadow edge point
6 | . BEGIN /* check whether it is in the shadow cast /
7 | . | Compute  $\beta$  /* Figure 9 /
8 | . | IF  $\beta < (90^\circ - \text{Elv.})$  &  $\{L_{i,c} \mid j < c < j'\} \in \text{shadow casts}$  then  $L_{i,j'}$  to be marked as shadow
9 | . END
10 | END
11 | Rotate back LiDAR raster with  $\theta = 270^\circ - \text{Az.}$ 
12 | Implement a morphology closing with a  $3 \times 3$  structure element /* to fill the
    | shadow gaps occurred by noise /
13 | Segment shadow pixels via N-8 neighborhood analysis
14 | For all shadow segments
15 | BEGIN /* shadow noise removal /
16 | . Compute the width and area
17 | . IF width < WidthTh or area < AreaTh THEN remove the shadow segment
18 | END
19 END

```

---

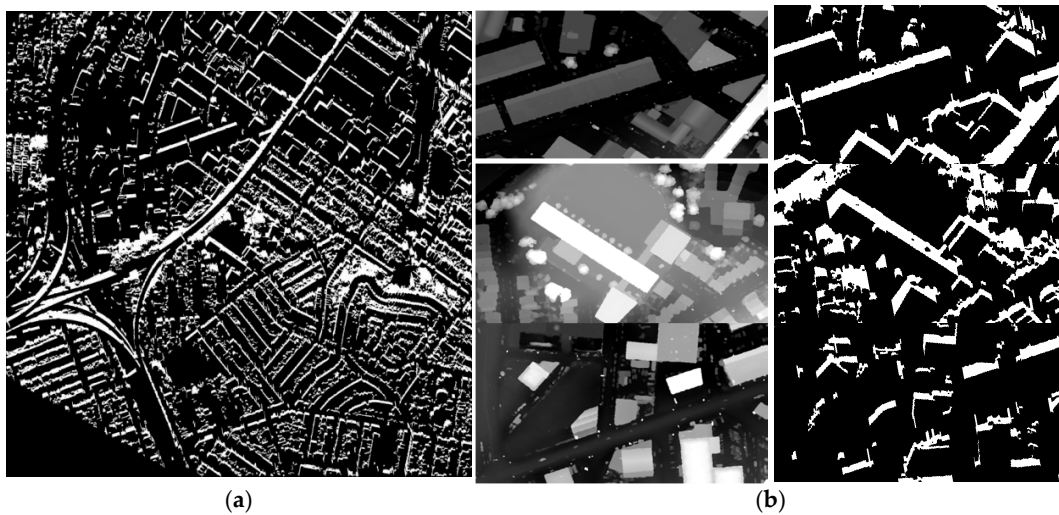


**Figure 10.** The shadow map extracted from the raster LiDAR data for the sample dataset: (a) Result of the overall application (white regions are shadows); (b) Enlarging the result of applying the algorithm on three regions alongside the LiDAR data.

In Figure 7 and Figure 10, comparable results can be observed as the obtained shadow maps in the LiDAR data and QB image. In other words, despite the different natures of the optic satellite image and LiDAR data, the same spatial topology of the occurrence of shadows was obtained.

Note that some of differences between the ISM and LSM are due to the spatial changes that occurred during the acquisition time difference between the LiDAR data and satellite imagery. This issue is more severe in the northwestern part of the sample dataset.

#### 4.2. Coarse 2D-Model Estimation

The obtained ISM and LSM, which are shadow masks of an identical region, are similar in content and general topology. Accordingly, it was decided to estimate a 2D-similarity transformation as the first registration attempt. This transformation is formulated below where  $\lambda$ ,  $[R_\theta]$  and  $[x_o, y_o]^T$  are the scale, 2D rotation matrix and translation vector respectively.

$$T(x, y) = \lambda \times [R_\theta] \times [x, y]^T + [x_o, y_o]^T \quad (18)$$

This transformation was expected to roughly relate the 2D digital coordinate systems of ISM and LSM. Considering that ISM ( $i, j$ ) and LSM ( $i', j'$ ) as conjugate positions, it is expected to have  $ISM(i, j) \approx LSM(T(i', j'))$ .

To do so, the method proposed by [34], in which the scale, rotation and translations of two images are determined via the detection of their maximum phase correlation in the frequency domain, was applied. In that method, a Shift Map (SM) is produced, which is equivalent to a 2D correlation map of an image ( $I_1$ ) with respect to the other one ( $I_2$ ). The maximum position of the SM is considered to be the most probable estimation for the existing shift between  $I_1$  and  $I_2$  (Equation (19)).

$$SM(I_1, I_2) = A \left( F^{-1} \left\{ \frac{F\{I_1\} \times F^*\{I_2\}}{A(F\{I_1\} \times F^*\{I_2\})} \right\} \right) \quad (19)$$

Here,  $F\{\}$  is the 2D Fast Fourier transform,  $F^{-1}\{\}$  is the inverse 2D Fast Fourier transform,  $A(\ )$  is the amplitude of the complex numbers, and  $*$  is the complex conjugate operator. Figure 11 show an example of SM between two sample images with shift difference.

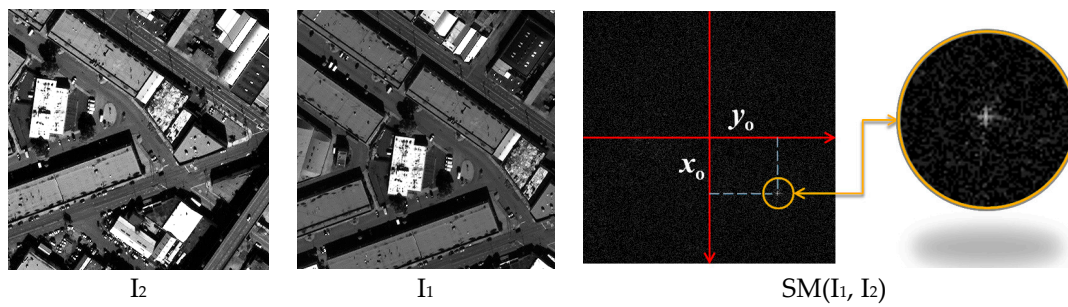


**Figure 11.** An example of SM between two sample images with shift difference.

To find the rotation and scale parameters,  $I_1$  and  $I_2$  should be mapped from Cartesian ( $x, y$ ) space to their Log-Polar ( $\log r = \log \sqrt{x^2 + y^2}$ ,  $\theta = \arctan \frac{y}{x}$ ) space (Figure 12). In this new space, the same model of Equation (19) leads to estimates of the scale and rotation parameters [34–36].

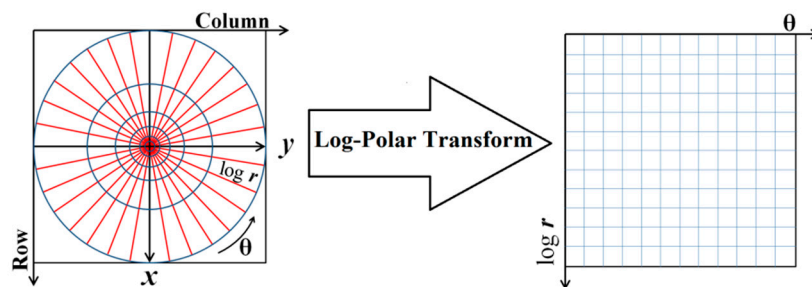


**Figure 12.** Schematic representation of the Log-Polar transformation.

Figure 13 shows schematically the concepts applied in the estimation of rotation and scale differences in the Log-Polar space. In this figure rotation and scale, applied on  $I_2$ , are computed with respect to  $I_1$ . In this regard, the rotated and scaled  $I_2$  would ultimately coincide with  $I_1$ .

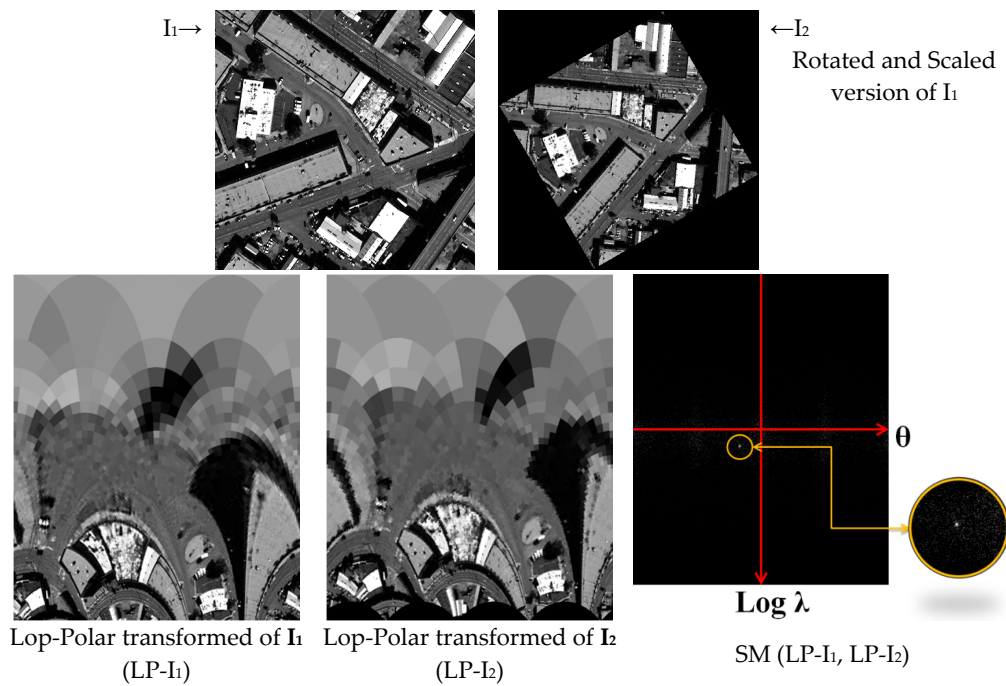


**Figure 13.** The estimation of rotation and scale difference between two images via the Log-Polar transformation.

The above procedure was implemented on the ISM and LSM by the following successive steps:

1. The logarithmic enhanced Fourier Spectrum of ISM ( $S_{ISM} = \log [A (F \{ISM\}) + 1]$ ) and LSM ( $S_{LSM} = \log [A (F \{LSM\}) + 1]$ ) were obtained. These spectrums ( $S_{ISM}$  and  $S_{LSM}$ ), which have scale and rotation differences from the origin ones [34], were mapped to Log-Polar space ( $LP-S_{ISM}$  and  $LP-S_{LSM}$ ), and the scale ( $\lambda$ ) and rotation ( $\theta_0$ ) parameters were solved via SM ( $LP-S_{ISM}$ ,  $LP-S_{LSM}$ ).
2. LSM was Scaled and Rotated (SR-LSM) to be consistent with ISM. The translation parameters were estimated between the ISM and SR-LSM images via SM(ISM, SR-LSM).

More details can be found in [34–36].

The estimated 2D-similarity parameters were finally implemented on the LSM to produce the Primary Transformed LiDAR Shadow Mask (PTLSM). The obtained result is presented in Figure 14.

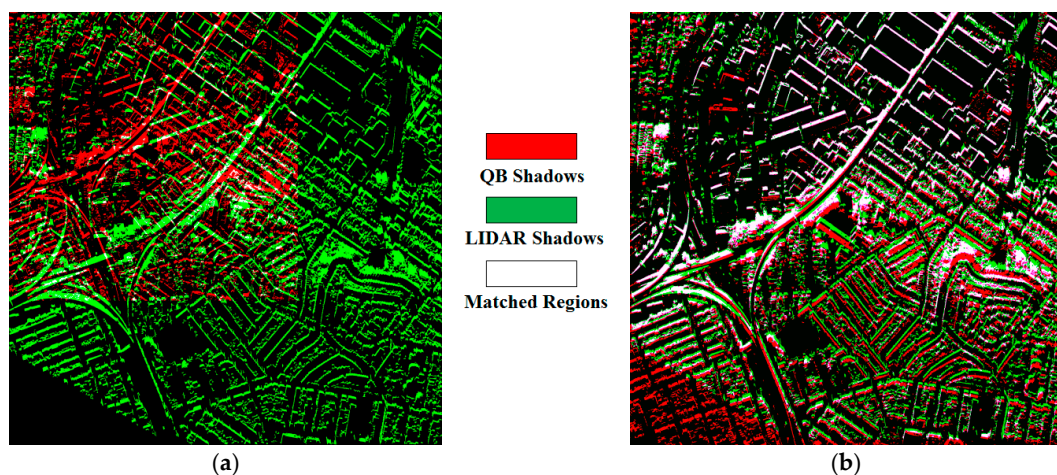


**Figure 14.** 2D-Similarity Transformation of the LSM to the ISM (Sample Dataset): (a) Before; (b) After.



Figure 14 shows that this 2D-similarity transformation is a very rough registration because there are significant geometric differences between the LiDAR data and optical images, which are mainly caused by relief changes. A detailed evaluation of this section is presented in Section 5.

#### 4.3. Fine 2D-Model Estimation

As seen above, the global 2D-similarity transformation is only an approximate model that leads to limited and non-uniform matched regions. This is a direct consequence of topography, which causes relief displacement in optical images, as well as different geometries in LiDAR data and optical image acquisitions. The accurate registration of LiDAR and images, however, requires vast and uniformly distributed matched points, which requires us to complement the coarse 2D-Model with a fine one. The fine model, which serves to improve the consistency between the LiDAR and image shadow masks, should be able to manage the remaining local distortions in the PTLISM.

In the applied method, the PTLISM was resampled to the Secondary Transformed LiDAR Shadows Mask (STLSM) via a 2D 7th-order polynomial (Equation (20)).

$$\begin{aligned}\Delta r &= \sum_{i=0}^7 \sum_{j=0}^{7-i} a_{i,j} r^i c^j \\ \Delta c &= \sum_{i=0}^7 \sum_{j=0}^{7-i} b_{i,j} r^i c^j\end{aligned}\quad (20)$$

Here,  $(r, c)$  are the 2D image coordinates of PTLISM and  $(\Delta r, \Delta c)$  are displacements between PTLISM positions and their corresponding ones in the ISM.

The coefficients of the polynomial ( $a_{i,j}$  and  $b_{i,j}$ ) were solved using least square method through a dense Displacements Map (DM) that represented the shifts  $(\Delta r, \Delta c)$  between all of the PTLISM pixels and their corresponding ones in the ISM. The provision of DM, which is the core concept of this section, is now explained.

Considering the local nature of the remaining distortions, a DM was generated in a hierarchical quad tree structure. To do so, the PTLISM and ISM were first divided into four parts, and the displacement vector (*i.e.*,  $\Delta r$  and  $\Delta c$ ) was estimated in each quarter (Equation (19)). Estimated  $\Delta r$  and  $\Delta c$  are duplicated to all positions of each quarter. The obtained DM was then updated in four more successive levels of the quad-tree. Figure 15 shows a diagram of the local shift updating for a typical quad-tree level.

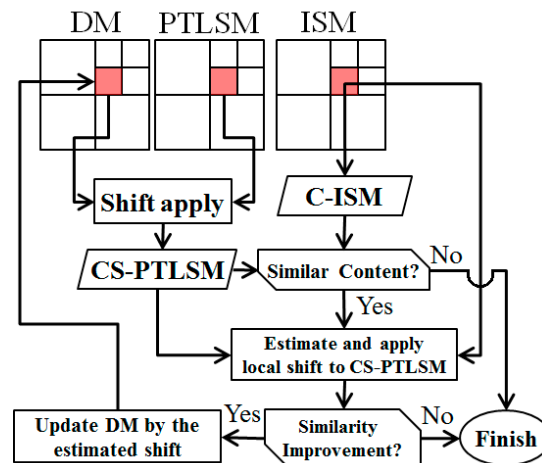


**Figure 15.** A diagram of the local shift updating for a typical quarter in a typical quad-tree level (here the 4th quarter of the 2nd level).

As Figure 15 shows, each working unit is composed of three coincident patches of the PTLISM, ISM and DM for a specific quarter in a specific quad-tree level. Among the three patches, the DM could be updated according to its relevant PTLISM and ISM ones.

The PTLISM was first shifted based on the displacement vectors included in the DM patch. The shifted PTLISM was then cropped (*i.e.*, a sub-matrix was extracted from PTLISM in the area defined by corresponding patch). This cropping yielded to a Cropped Shifted PTLISM (CS-PTLISM).

The relevant ISM patch was also cropped from the original ISM, which was named the Cropped ISM (C-ISM). These two patches were compared and the dissimilarity measure,  $\Gamma$ , was computed (Equation (21)). This measure ranges between [0~1] and characterizes the difference level between two binary maps from the consistency perspective between true-valued pixels.

$$\Gamma = \frac{2 \times |\text{Nr}(\text{C-ISM}) - \text{Nr}(\text{CS-PTLSM})|}{\text{Nr}(\text{C-ISM}) + \text{Nr}(\text{CS-PTLSM})} \quad (21)$$

Patches with  $\Gamma < 0.5$  are thought to be similar enough to be used for shift estimation via Equation (19) and in the same manner explained in Section 4.2 (the maximum position in the SM locates the shift parameters). The estimated shift parameters were applied to the CS-PTLSM and, afterwards, the effectiveness of this shift was evaluated in terms of the similarity improvement between CS-PTLSM and C-ISM. To do so, the following measure,  $\Theta$  in Equation (22), was computed before and after applying the shift. If  $\Theta$  indicated a similarity improvement, the estimated values were added to the current values of the DM.

$$\Theta = \frac{2 \times \text{Nr}(\text{C-ISM}) \cap \text{CS-PTLSM}}{\text{Nr}(\text{C-ISM}) + \text{Nr}(\text{CS-PTLSM})} \quad (22)$$

This measure, which again ranges between [0~1], characterizes the coincident areas between two binary maps, here CS-PTLSM and C-ISM.

In the above-mentioned procedure, a DM, which is a dense map developed by conjugating the PTLSM and ISM, was generated (one  $\Delta r$  and one  $\Delta c$  for almost all PTLSM pixels). The final 7th-order polynomial was computed based on the DM to give a continuous and smooth mapping function between the PTLSM and ISM (Equation (20)). This polynomial was ultimately applied to resample the PTLSM to the STLSM. Figure 16a shows the estimated displacements through the polynomials, and Figure 16b presents the obtained STLSM.

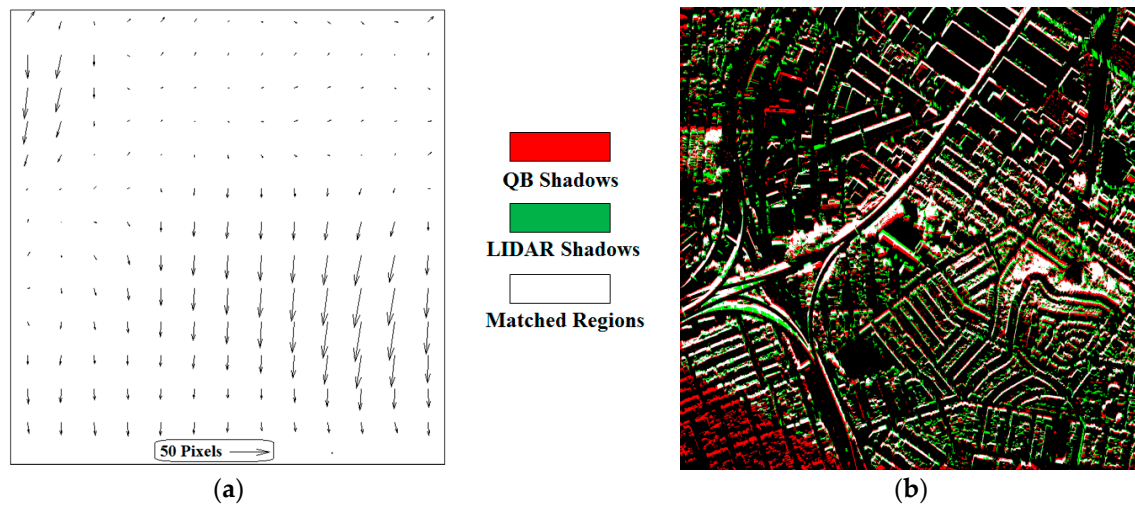


**Figure 16.** Displacement vectors obtained from the fine 2D model and the result of the matching between the ISM and STLAM: (a) 2D Displacements Map; (b) Compliance of the STLSM and ISM.

Correction vectors ( $\Delta r$ ,  $\Delta c$ ) were computed for a regular grid of points in PTLSM. For this reason the fitted polynomial of Equation (20) was applied. These vectors are depicted in Figure 16a. These vectors show the magnitude and orientation of the corrections in PTLSM. A comparison between Figure 14b and Figure 16b reveals the significant improvement achieved in this section.

#### 4.4. Coarse 3D-Model Estimation

The registration model between the 3D LiDAR grid data and 2D pixels of the satellite imageries should be a 3D model, such as the well-known 3D-Affine. However, what we have obtained so far is a 2D global polynomial between the LiDAR and image shadow masks.

In this section, the matched shadow masks are segmented to local shadow patches first and then the local shifts between relevant segments are estimated and removed. A set of matched points between the 3D-LiDAR

data and 2D satellite image are then obtained via the locally shift removed shadow segments. The points are filtered to omit blunder ones and finally a 3D affine model is fitted to the remaining ones as the coarse registration 3D model. Figure 17 shows a flowchart of this section.

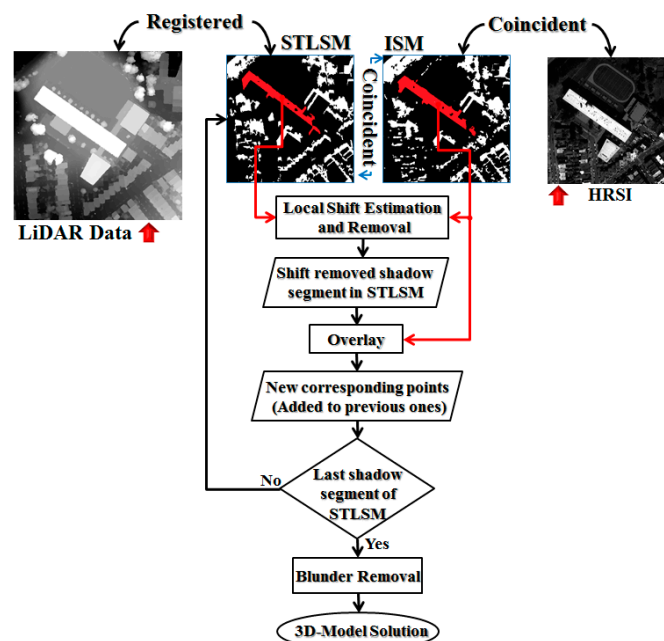


**Figure 17.** Flowchart of the individual shadow segment matching and coarse 3D-Model estimation.

As shown in the above figure, HRSI is coincident with its ISM, while LiDAR data are registered to STLSM. In other words, each pixel in the STLSM can be mapped to its correspondent LiDAR point via the consecutive inverse transformations in Figure 18.

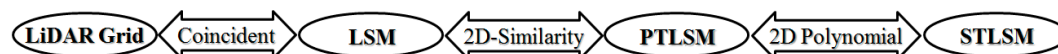


**Figure 18.** Mathematical relations among the 2D Transformed LiDAR shadow masks.

The STLSM, which contains shadow pixels in the same coordinate system as the ISM, was first segmented via an N-8 neighborhood analysis. For each shadow segment, the relevant shadow segments in the ISM were found, and the shift parameters were estimated as the maximum position in their Shift Map (see Section 4.2). These shifts, which were specifically assigned to one shadow segment of the STLSM, were then inversely applied, and the shift-removed segments were overlaid with the ISM. The 2D image coordinates of the overlaid ISM pixels accompanied by the 3D coordinates of the relevant STLSM points made up a set of corresponding points (see Figure 17).

Performing the above-mentioned procedure for all of the shadow segments of the STLSM, a rather vast set of corresponding points was provided between the LiDAR and HRSI. However, these points included incorrect and inaccurate points, primarily due to the imperfection of the LiDAR and/or HRSI shadow mask generation, the time difference between the LiDAR and HRSI and the vertical displacements in the HRSI. Therefore, a 3D-affine model was first fitted to all of the initial correspondent points (Equation (1)), and the residual vectors were obtained. Next, the initial correspondent points were reduced to half by omitting the points with large residual vectors. The remaining points were finally applied to solve the coarse 3D-Affine model between the LiDAR data and HRSI ( $M^{\text{Coarse}}$ ).

The obtained coarse 3D-affine model was evaluated from two points of view: absolute and relative evaluations. In the absolute evaluation, the GCPs (Section 3) were directly used. The 3D coordinates of the GCPs were placed on the obtained 3D-Affine, and their absolute residual vectors were computed in the image space. Conversely, for the relative evaluation, a comparison was made between the obtained 3D-Affine model ( $M^{\text{Coarse}}$ ) and the desired accurate 3D-Affine model solved via the GCPs ( $M^{\text{Ctrl}}$ ). For this reason, each LiDAR

grid point was transformed to the image space once with the coarse 3D-Affine and once with the control one (*i.e.*, solved by the GCPs). The image coordinate was then compared as the relative residual vectors  $[\delta r, \delta r]^T = [M^{Ctrl} - M^{Coarse}] \times [X, Y, Z, 1]^T$ . Figure 19a shows the absolute and relative residual vectors together. The absolute evaluation results are reported in Table 2, and Figure 19b shows a histogram of the relative residual vector lengths.

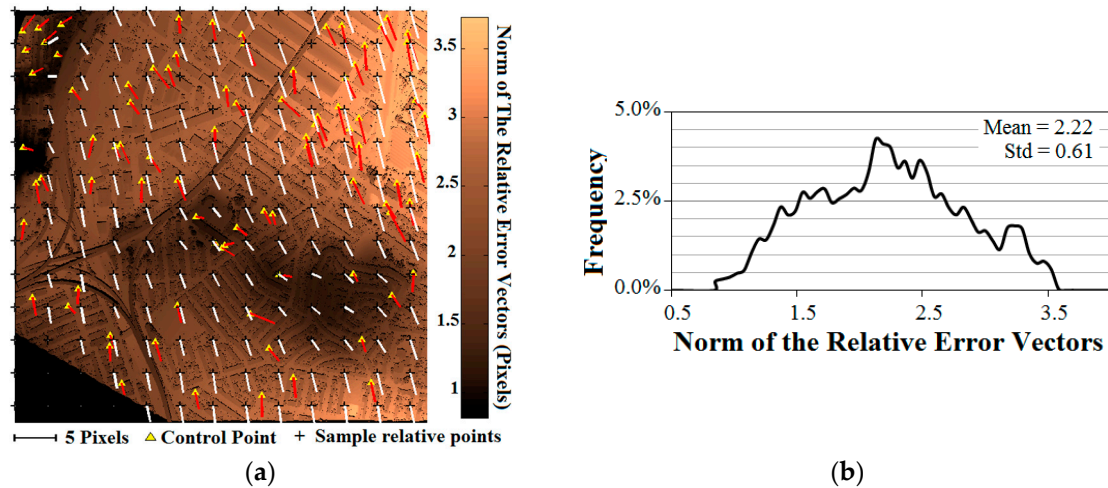


**Figure 19.** Absolute and relative error vectors with a histogram of the relative errors for the sample dataset: (a) Sizes and orientations of the error vectors; (b) Length histogram of the relative error vectors.

**Table 2.** RMSE of the sample dataset's control points estimated by the Coarse 3D-Model.

RMSE in Rows	2.21 Pixels
RMSE in Columns	0.97 Pixels
Total RMSE	2.41 Pixels

In Figure 19a, 84 control points of sample dataset are shown by yellow triangles. In this figure, error vectors at each control point, estimated via the coarse 3D-model, are presented by red lines. In addition, the relative error vectors between control model and the obtained coarse 3D-model are depicted via white lines organized in a regular grid. The norm of the relative error vectors at the image positions are represented by the gray scale value of this figure.

According to Table 2 and Figure 19b, the absolute and relative residual vectors are less than 2.5 and 4 pixels, respectively, which is very promising for a coarse model. However, the relative residual vectors in Figure 19a show systematic behaviors that indicate the presence of un-removed systematic errors. The correction of this error source is the subject of the next section.

#### 4.5. Fine 3D-Model Estimation

This section is aimed at improving the coarse 3D model ( $M^{Coarse}$ ) into a fine one ( $M^{Fine}$ ) via an iterative method. The underlying idea was a dense edge-based matching between the image and LiDAR, which would yield a rich set of matched points (the 2D image points and the 3D LiDAR points). These points were finally applied to solve a fine 3D model.

Edges were extracted from the optical images using a standard Canny operator (PAN\_Edges). The LiDAR edges (LS\_Edges), on the other hand, were obtained from two sources: the Canny operator on the LiDAR grid (the pixels in which an abrupt elevation change occurs) as well as shadow edges obtained via an edge detection from the LSM (Equation (23)).

$$LS\_Edges = \{[X, Y, Z]^T \in (LiDAR\ Edges \cup LSM\ Edges)\} \quad (23)$$

The elevations of these 3D shadow points were extracted as the maximum elevation in a  $3 \times 3$  window around each point.



The edges, which were differently interpreted in the LiDAR data and optical images, are more likely to occur in the image. Accordingly, the LiDAR edges were considered as the base, and their corresponding positions were searched for in the image.

In each iteration step, the LiDAR edges were transformed to the image space via the last 3D model (initialized with the  $M^{\text{Coarse}}$  of Section 4.4). This transformation not only makes the two data sets geometrically consistent but also brings their corresponding edges in the vicinity of each other. Nearly positioned corresponding edges suggested the utilization of Iterative Closest Edge Points Matching (ICEPM). This technique was inspired from the well-known Iterative Closest Points (ICP), in which 3D cloud points taken from different viewpoints are matched together [37]. The ICP and subsequently the ICEPM, however, need the approximate transformation parameters between the datasets. The iterative procedure applied to improve the 3D affine model via the ICEPM is presented in the next page pseudocode entitled as Algorithm 3.

As mentioned, the 3D LiDAR edge pixels (from the LiDAR grid edges and shadow edges taken from the LSM) were projected onto the image space via the last 3D model ( $M^{\text{Last}}$ ) in hand. The projected LS\_Edges were named PLS\_Edges.

The PLS\_Edges were divided into  $k = n \times m$  regular patches (line 4) to facilitate the management of the local systematic errors. The parameters  $n$  and  $m$  were selected to yield  $k = 100$  patches. These patches were expanded with a 10-pixel margin in the PAN\_Edges image to ensure the presence of corresponding edges (line 7).

Considering the unbalanced number of extracted edges from the image and LiDAR and also the expectation to have PLS\_Edges in the vicinity of their corresponding PAN\_Edges, the *DistTh* threshold (line 11) was used to prevent mismatched points. This threshold was set to 10 pixels.

The convergence criterion in line 15 was evaluated in terms of the absolute values of the 2D similarity parameters, namely the translations and the rotation angle, which were expected to be close to zero. For the estimated scale parameter, values close to one are expected. However, it is recommended that a maximum number of iterations should be set for probable biased cases.

After the convergence of the ICEPM, which was executed for each patch, the obtained matched pairs closer than the *MatchTh* threshold were selected as the appropriate pairs of that patch. Each pair was comprised of the 2D positions of an edge pixel in PLS\_Edges, and its corresponding positions in the source PAN\_Edges (*i.e.*, the PAN\_Edges before the 2D transformations of the ICEPM). *MathTh* was set cautiously to 1.5 pixels because the 2D similarity model cannot manage all of the local distortions.

The ICEPM was performed on all the  $n \times m$  patches, and the obtained matched pairs were integrated into a unique set (line 18). These matched points were then segmented via the N-8 neighboring analysis performed on the PLS\_Edges, which led to continuous and isolated groups of points. Longer segments were considered to more reliably contain true and accurate matched pairs. Accordingly, the squared length of each segment was set as the initial impact weight associated with all of its points (line 19–20). These weights, which were assigned to all matched pairs, were organized in the form of a weight matrix that was later applied in the robust estimation of a 3D affine model relating the LiDAR data and the HRSI (line 21). A robust estimation was implemented to manage the blunders probably existed among the selected matched pairs. The details of this technique are presented below.

The main goal in the robust estimation technique is to reduce the effect of incorrect or inaccurate observations in a particular solution. Among the different robust estimation techniques, Variance Components Estimation (VCE), which is based on proper weighting of observations [38], was applied.

In the process of the least square estimation, the VCE categorized the vector of observations ( $l$ ) and its corresponding covariance matrix ( $C_{ll}$ ) into the  $k$  homogeneous groups ( $l = [l_1, l_2, \dots, l_k]^T$ ) and estimated the variance components associated with each group (Equation (24)).

$$C_{ll} = \sum_{i=1}^k \sigma_i^2 Q_i, \quad Q_1 = \begin{pmatrix} [q_1] & 0 & \dots & 0 \\ & 0 & & 0 \\ & & \ddots & \vdots \\ & & & 0 \end{pmatrix}_{n \times n}, \quad Q_2 = \begin{pmatrix} 0 & 0 & \dots & 0 \\ & [q_2] & & 0 \\ & & \ddots & \vdots \\ & & & 0 \end{pmatrix}_{n \times n} \dots Q_k = \begin{pmatrix} 0 & 0 & \dots & 0 \\ & 0 & & 0 \\ & & \ddots & \vdots \\ & & & [q_k] \end{pmatrix}_{n \times n} \quad (24)$$

In Equation (24),  $C_{ll}$  is the covariance matrix of observations;  $k$  is the number of homogenous observations sets (NrHOS);  $Q_i$  ( $i = 1, 2, \dots, k$ ) are square  $n \times n$  matrices ( $n$  is number of whole observations,  $\sigma_i^2$  is a variance component of  $i^{\text{th}}$  homogenous observations set and  $q_i$  ( $i = 1, 2, \dots, k$ ) are sub-matrices from the cofactor matrix.

**Algorithm 3** ICEPM and Fine 3D-Model Estimation

Input: LiDAR grid data

Panchromatic Edges (PAN\_Edges)

LiDAR &amp; Shadow Edges (LS\_Edges)

Coarse 3D-Model ( $M^{\text{Coarse}}$ )Number of regular grids in row ( $n$ ) and column ( $m$ ) directionThresholds ( $DistTh$ ,  $MatchTh$  &  $ModelTh$ )Output: Fine 3D-Model ( $M^{\text{Fine}}$ )

---

```

1   $M^{\text{New}} \leftarrow$  Set the  $M^{\text{Coarse}}$  as the New Model
2  BEGIN /* 3D-Model Refinement */
3  |  $M^{\text{Last}} \leftarrow$  Set the  $M^{\text{New}}$  as the Last Model
  |  $PLS\_Edges = \{[r_l, c_l]^T = [M^{\text{Last}}] \times [X, Y, Z, 1]^T \mid [X, Y, Z] \in LS\_Edges\}$ 
4  | Divide  $PLS\_Edges$ 's extent into the non-overlapped  $k = n \times m$  regular patches
  | ( $P = \{p_1, p_2, \dots, p_k\}$ ) /*  $p_i$  is the  $i^{\text{th}}$  patch boundary */
5  | FOR all  $P = \{p_1, p_2, \dots, p_k\}$ 
6  | .  $PLS\_Edges_i \leftarrow \{[r_l, c_l]^T \in p_i\}$ 
7  | .  $PAN\_Edges_i \leftarrow \{[r, c]^T \in \text{expanded } p_i\}$  /* to ensure correspondences would be included */
8  | . BEGIN /* Iterative Closest Edge Points Matching (ICEPM) */
9  | . | FOR each  $PLS\_Edges_i$  point
10 | . | .  $d \leftarrow$  distance to the nearest  $PAN\_Edges_i$  point
11 | . | . IF  $d < DistTh$  THEN set the edge point as the correspondence
12 | . | . END
13 | . | Estimate a 2D-similarity model using all correspondent points
14 | . | Update the  $PAN\_Edges_i$  using the estimated 2D-similarity model
15 | . | DO UNTIL 2D-similarity parameters are converged
16 | . | Choose the  $i^{\text{th}}$  set of matched points based on  $d < MatchTh$  threshold
17 | . END
18 | Integrate all matched points
19 | Segment all matched  $PLS\_edges$  pixels via N-8 neighborhood analysis
20 | Initialize the weights for matched points of each segment
21 | Robust estimation of 3D-Model coefficients using matched points (Next pseudocode)
22 |  $M^{\text{New}} \leftarrow$  Set the estimated 3D-Model as the New Model
23 |  $REVM \leftarrow$  Compute the Relative Error Vectors Map between  $M^{\text{Last}}$  and  $M^{\text{New}}$  (Equation (26))
  DO UNTIL  $\max(|REVM|) > ModelTh$ 
24 Set the NM as the ( $M^{\text{Fine}}$ )

```

---

Considering  $W = C_{ll}^{-1}$  as the weight matrix of the observations, the variance component of each homogenous observations set ( $\sigma_i^2$ ,  $i = 1, 2, \dots, k$ ) is computed using the approximate initial weights as follows (Equation (25)).

$$\hat{\sigma}_i^2 = \frac{v_i^T W_i v_i}{n_i - \text{tr}((B^T W B)^{-1} B_i^T W_i B_i)} \quad i = 1, 2, \dots, k \quad (25)$$

In Equation (25),  $v_i$  is the residuals vector of the  $i^{\text{th}}$  homogenous observations set.  $W_i$  and  $B_i$  are the sub matrices from the weight and design matrices, respectively; they are related to the  $i^{\text{th}}$  homogenous observations set.  $\text{tr}$  is the trace operator and  $n_i$  is the number of members in the  $i^{\text{th}}$  homogenous observations set.

This process was iteratively performed on all of the homogeneous groups of observations and assigned different impact weights to each group until the  $\sigma_i^2$  values converge to one. As a result, each observation group had an adjusted impact that was proportional to its weight for the estimation of the unknown parameters. See [38,39] for additional theoretical details.

The separation of the observations into homogeneous groups comprises the core concept of the VCE. In our application, the matched points were categorized according to their residual vectors in the least squares estimation of the relating 3D model (*i.e.*, the 3D affine in our case). This process began with 2 observation sets and increasingly continued until no significant effect occurred in the estimated 3D-affine model. The details of this process are presented in the Algorithm 4.

The purpose of each iteration step was to categorize the matched point pairs into an increasing Number of Homogeneous Observation Sets (NrHOS). It began by the computing residual vectors for all of the pairs using the last 3D model (line 6). The lengths of the residual vectors were normalized in the range of [1~10]. This range was transformed to a logarithmic scale and was then divided into NrHOS equal parts. Afterwards, the matched pairs were categorized to the NrHOS sets based on the length of their residual vectors (line 7–9).

The logarithmic partitioning of the normalized residuals' lengths (line 8) is a cautious technique for classifying points into homogeneous groups. Figure 20 schematically depicts the division ranges for the different homogeneous groups obtained for NrHOS from 2 to 20.

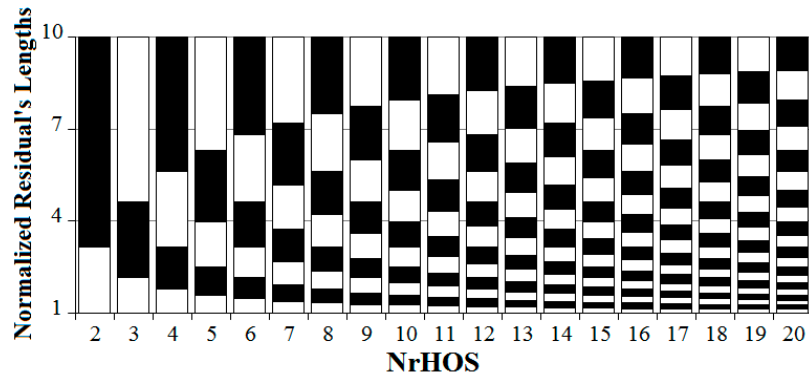


**Figure 20.** The range of the residual vectors lengths associated with each homogeneous set for different values of NrHOS from 2 to 20.

---

**Algorithm 4** Robust Estimation of the 3D-Model Coefficients

---

Input: LiDAR grid

Matched Points (image points  $(r, c)$  and the corresponding 3D LiDAR positions  $(X, Y, Z)$ )

Initial weight matrix of the image observations ( $\mathbf{W}$ )

$ModelTh$

Output: Coefficients of the 3D-Model

---

```

1   $M^{New} \leftarrow$  Set the estimated 3D-Model using  $\mathbf{W}$  as the New Model
2   $NrHOS = 1$  /* Number of the Homogeneous Observation Set /
3  BEGIN /* Robust Estimation of 3D-Model Coefficients /
4  |  $M^{Last} \leftarrow$  Set the  $M^{New}$  as the Last Model
5  |  $NrHOS \leftarrow NrHOS + 1$ 
6  |  $\vec{v} \leftarrow$  Compute the residual's length vector using the  $M^{Last}$ 
7  |  $n\vec{V} \leftarrow$  Normalize  $\vec{V}$  in the range of [1~10]
8  | Divide the  $n\vec{V}$  into the isometric NrHOS categories on the logarithmic scale (Figure 20)
9  | Set the corresponding Matched Points of each categories as an Homogeneous
   | Observation set
10 |  $\mathbf{W} \leftarrow$  Update the  $\mathbf{W}$  using the VCE technique (Equations (24) and (25))
11 |  $M^{New} \leftarrow$  Set the estimated 3D-Model using  $\mathbf{W}$  as the New Model
12 | REVM  $\leftarrow$  Compute the Relative Error Vectors Map between  $M^{Last}$  and  $M^{New}$  (Equation (26))
13 DO UNTIL  $\max(|REVM|) > ModelTh$ 
14 Set the  $M^{New}$  as the coefficients of 3D-Model

```

---

In Figure 20, each bar refers to a specific number of homogeneous observation sets (NrHOS) in the VCE method. The vertical axis shows the normalized range of error vector lengths computed from the least-square solution. Each bar is divided into NrHOS black-and-white parts, each of which indicating to the range of error vector lengths considered for each individual set of homogeneous observations.

The convergence criterion was estimated through a Relative Error Vectors Map (REVM), in exactly the same way as the previous pseudocode (Algorithm 3). The REVM was comprised of displacement vectors  $([\delta r, \delta c])$  between the image positions computed once by the  $M^{Last}$  and once by the  $M^{New}$  (Equation (26)).

$$[\delta r, \delta c]^T = [M^{New} - M^{Last}] \times [X, Y, Z, 1]^T \quad (26)$$

The maximum length of these vectors should be less than *ModelTh* to stop the iterations. This threshold was set to 0.1 in the robust estimation of the 3D-Model coefficients algorithm (Algorithm 4) and to 0.9 in the ICEPM and the fine 3D-model estimation algorithm (Algorithm 3).

The fine 3D model estimation, similar to the coarse one, was evaluated from two relative and absolute aspects. Figure 21a shows the relative and absolute error vectors. In this figure, the relative error vectors are estimated on a regular grid, where their sizes are depicted as different gray level tones. A histogram of these vectors is also presented in Figure 21b. Furthermore, the absolute evaluation parameters obtained by using manually extracted control points are reported in Table 3.

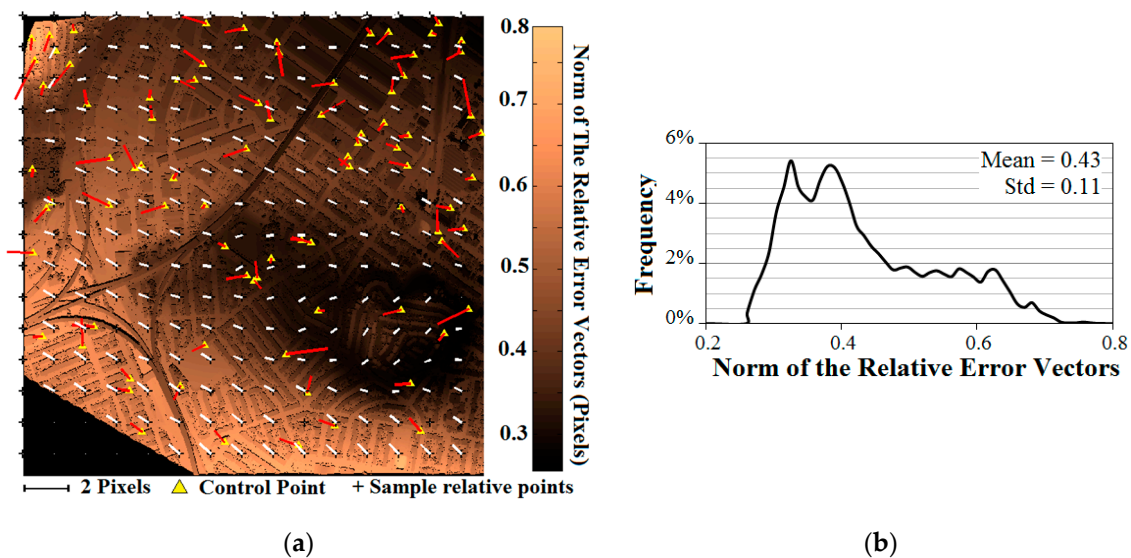


**Figure 21.** Absolute and relative error vectors with a histogram of the relative errors for the sample dataset: (a) Sizes and orientations of the error vectors; (b) Length histogram of the relative error vectors.

**Table 3.** RMSE of the sample dataset's control points estimated using the Fine 3D-Model.

RMSE in Rows	0.54 Pixels
RMSE in Columns	0.64 Pixels
Total RMSE	0.84 Pixels

Figure 21a has the same structure of Figure 19a, but in this case all the error vectors (*i.e.*, absolute ones on control points with red color as well as white-color relative ones) are computed via fine 3D-model. Again gray scale at each position represents the norm of the relative error vector, here for the fine 3D-model.

The histogram shown in Figure 21b, when compared to its equivalent in Figure 19b, shows a significant improvement for the fine 3D model *versus* the course one. According to this histogram, the norms of all of the relative error vectors were smaller than one pixel, and thus, their quasi-systematic behavior can be easily ignored. Furthermore, the absolute evaluation parameters demonstrated the success of the ultimate fine 3D model for the registration of the LiDAR data to the HRSI.



## 5. Discussion and Evaluations

### 5.1. Evaluation of the Consistency between LiDAR and Image Shadows

Our hierarchical method can be thought of as successive steps in which the geometrical consistency between the LSM and ISM was sequentially improved. This process can be summarized by its product chain, which is presented in Figure 22.

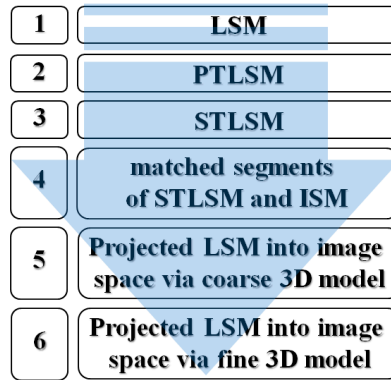


**Figure 22.** Product chains in the process of coinciding the LSM with the ISM.

The coincidences of these six products with the ISM were evaluated via three indices: the Image based Matching Factor (IbMF), LiDAR based Matching Factor (LbMF) and Average based Matching Factor (AbMF). These indices are introduced in Equations (27)–(29), respectively.

$$\text{IbMF} = \frac{\text{Nr}(\text{ISM} \cap \text{LIDAR Shadows})}{\text{Nr}(\text{ISM})} \quad (27)$$

$$\text{LbMF} = \frac{\text{Nr}(\text{ISM} \cap \text{LIDAR Shadows})}{\text{Nr}(\text{LIDAR Shadows})} \quad (28)$$

$$\text{AbMF} = \frac{2 \times \text{Nr}(\text{ISM} \cap \text{LIDAR Shadows})}{\text{Nr}(\text{ISM}) + \text{Nr}(\text{LIDAR Shadows})} \quad (29)$$

In the above equations, the six successive products of Figure 22 were replaced by “LiDAR Shadows” one-by-one, and the three indices were computed for them. The obtained results are presented in Figure 23. In this figure, the horizontal axis shows the numbers of products in the chain of Figure 22.

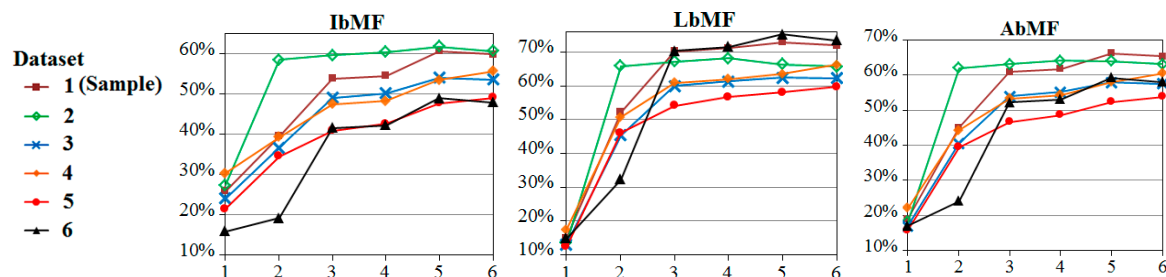


**Figure 23.** Coincidence evaluation between the LiDAR shadow products (in the chain in Figure 22) and the ISM.

Figure 23 obviously shows an improving trend in the consistency between the LiDAR shadows and the ISM during the product chain. A more detailed examination reveals that the PTLSM and STLSM contained the highest improvement level of this product chain. The lower accuracy in dataset No. 5 was primarily the result of the lower coverage between the LiDAR data and the optical image for this dataset.

As seen, the LbMF was higher than the IbMF for 10% in all datasets on average. Three reasons can be assigned to this fact. First, the QB images were not fully covered by the LiDAR data, leading to some image shadows with no equivalent in the LiDAR. Second, some image shadows were placed in the height displacement regions (e.g., the side walls of buildings in urban areas), whereas those shadows cannot be reconstructed from the LiDAR data. Third and finally, in some cases water and other dark objects were wrongly detected as shadows, which certainly have no conjugate in the LiDAR data.

## 5.2. Evaluation of Registrations through the 3D Models

In this section, the absolute accuracies of the coarse and fine 3D models, characterized in terms of the RMSE, were evaluated for all of the data sets. For that reason, the manually extracted control points were used as the independent sources for the comparison. The results are reported in Table 4. The fine 3D model, the evaluation of which is shown on the right side of Table 4, indicates an accurate registration between the LiDAR and image on the order of 1 pixel.

**Table 4.** RMSEs of the coarse and fine 3D models.

Dataset	Coarse 3D Model			Fine 3D Model		
	Row	Column	Total	Row	Column	Total
1 (Sample)	2.21	0.97	2.42	0.54	0.64	0.84
2	2.28	1.17	2.56	0.81	0.90	1.21
3	2.54	1.22	2.82	0.82	1.01	1.30
4	3.53	2.68	4.43	0.92	0.91	1.29
5	3.29	0.80	3.39	0.81	0.62	1.02
6	1.94	0.94	2.16	0.68	0.78	1.03

The comparison between the fine and coarse 3D models demonstrates the significant improvement of the fine model *versus* the coarse one. To make a more detailed comparison, the displacement vectors between the fine and coarse models were obtained for the entire region of each data set. Histograms of the lengths of these displacement vectors are shown in Figure 24.

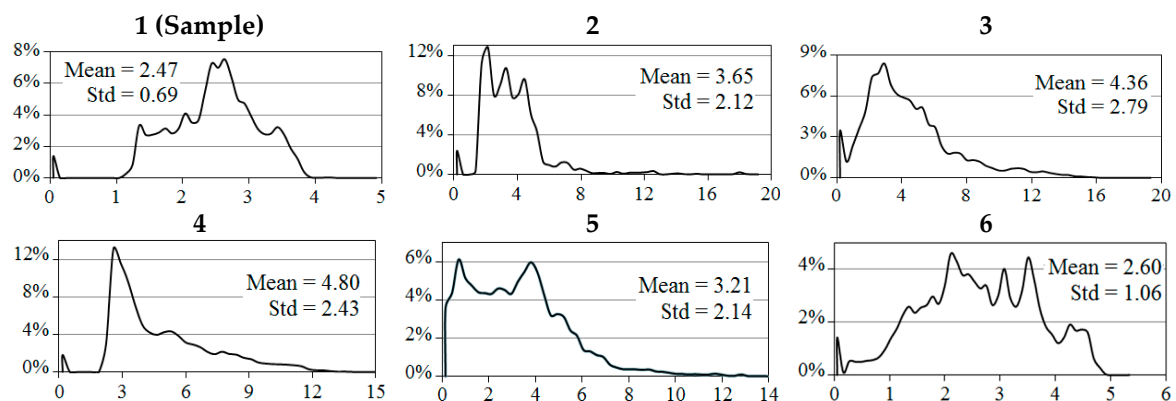


**Figure 24.** Histograms of the lengths of the displacement vectors between the coarse and fine 3D models for all of the data sets.

A first look at Figure 24 may suggest that the fine model only had a mean improvement of less than 4 pixels. However, it should be noted that some regions had large displacement vectors, even larger than 10 pixels, which were corrected by the fine model. Figure 25 shows some examples. In the figure, the LiDAR edges, which were transformed to the image space by the coarse 3D model, are shown in green, and the red ones show the edges that were transformed by the fine model.





**Figure 25.** Some examples of the large differences between the coarse and fine 3D models.

Figure 25 shows the necessity of the fine 3D model as well as the ICEPM. Both are essential to compensate for regions where the performance of the coarse model is far from that desired.

For visual inspection, the ultimate result of the proposed method is presented in Figure 26. In this figure, PLS\_Edges, which represents the LiDAR and shadow edges projected via the fine 3D model into the image space, is shown in red and is superimposed on the optical image.

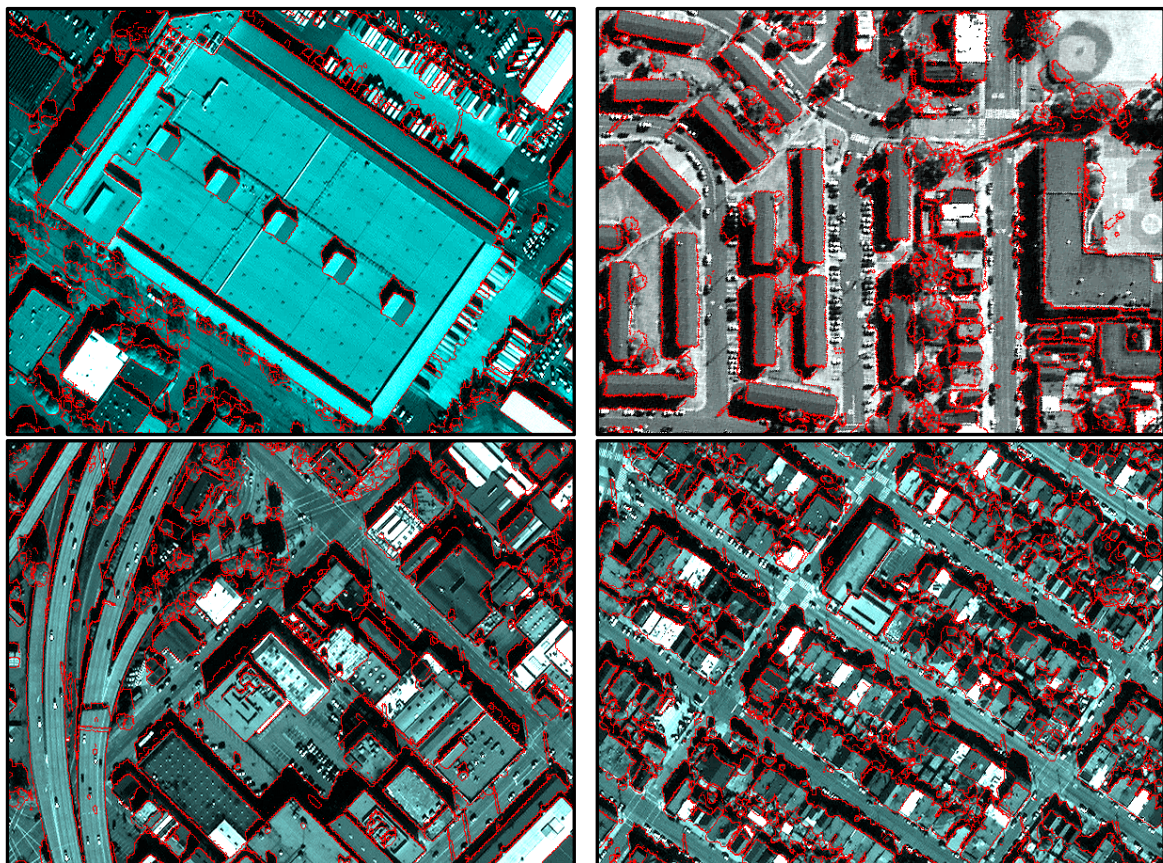


**Figure 26.** Projected LiDAR and shadow edges transformed and superimposed on the HRSI via the fine 3D model.

The satisfactory coincidence of the LiDAR edges with their corresponding ones in the optical image demonstrates the efficiency of the proposed method as well as its applicability in dense urban areas.



### 5.3. Discussion on the Changed Regions

Changed regions are one of the uncertainty sources in the automatic registration methods. In Figure 27, PLS-Edges are shown for some instances of the changed regions (the same regions previously presented in Figure 2). These edges are superimposed on the optical image via the ultimate fine 3D-model.

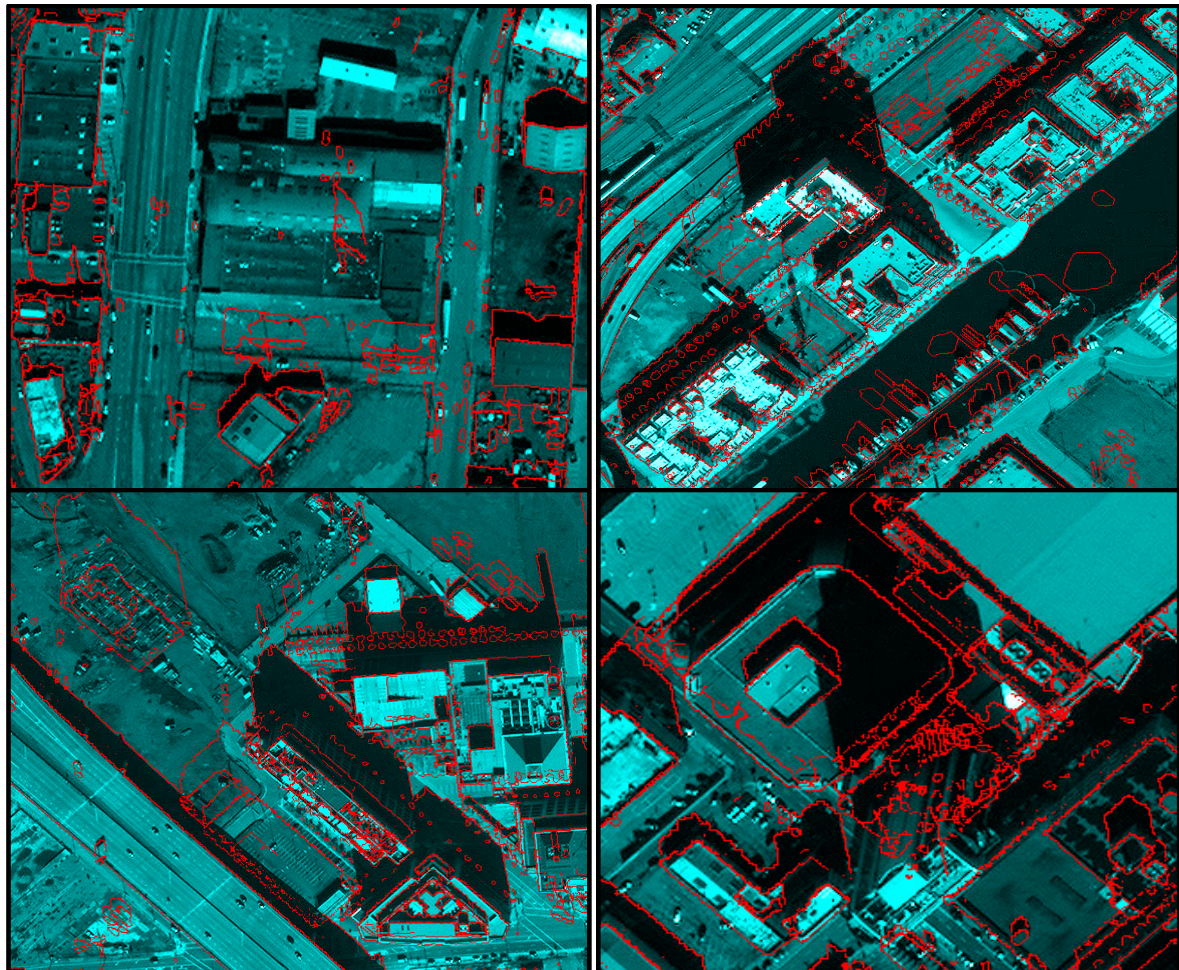


**Figure 27.** Samples of the PLS\_Edges via the fine 3D model (red edges) superimposed on the HRSI in changed regions (similar regions with Figure 2).

As the above figure shows, unmatched shadow edges, which are mainly caused by occlusions and changed regions, did not have a destructive effect on the final results even in adjacent regions. In other word, true edges are precisely coincident even with the presence of some unmatched shadow edges. This robustness can be justified by 1-the limited number of parameters in the fine model (*i.e.*, 8 parameters of 3D affine which prevent the over-parameterization problem), 2-the length-based weighting of corresponding edges in Section 4.5 (ICEPM and Fine 3D-Model Estimation) and 3-robust estimation and blunder removal via the iterative VCE procedure (Robust Estimation of the 3D-Model Coefficients).

## 6. Conclusions

The core of each registration is the extraction of common features from each source that can be used as prospective matching candidates. For LiDAR to image registration, however, these common features are the primary challenge because these two data sources have totally different geometric and radiometric contents.

In this paper, shadows, which are highly frequent features in urban and rural areas, were used as matching features. For that reason, the existing methods for shadow extraction from LiDAR and optical images were developed, and two shadow masks were obtained automatically. The remaining steps were mainly devoted to



the compensation of geometric differences between the two shadow masks. To do so, an automatic hierarchical method, which included four consecutive steps, was designed. In the proposed hierarchical method, the LiDAR shadows were mapped to their matched shadows in the image. A dense set of corresponding pairs between the 3D LiDAR data and 2D image pixels was thus obtained. These points were ultimately applied to solve a fine registration 3D model, which was herein a 3D-affine. The obtained results, which were evaluated for 6 different data sets, showed very promising results that had approximately one pixel accuracies or better.

The main characteristic of the proposed method is its independence from any initial information or user guidance (e.g., RPCs an initial relating models). This method offers a major contribution because all of the previous methods rely on at least a rough initial model between the LiDAR data and optical image.

The proposed method was resistant to changes arising from the time differences between the two data sets. This makes the method applicable in urban areas, even with a time lag between the LiDAR data and HR image. This characteristic was demonstrated because there was a 3-year interval between the LiDAR data and HRSI used in this paper.

The proposed method was implemented in the MATLAB and was run with an ordinary desktop computer (using an Intel Core2 2.4-GHz central processing unit with a memory of 4 GB). This MATLAB code takes on average 25 min run-time which can be certainly improved in professional programming languages or using faster computers.

## 7. Future Works

The extension of this method to medium-resolution satellite imagery or low-density LiDAR data is suggested for further research.

Among different similarity measures those driven from information theory have been more promising between LiDAR data and optical images. With absence of an initial relating model, the application of these measures (e.g., mutual information) in a multi-resolution registration hierarchical approach is suggested for further study.

**Acknowledgments:** The authors would like to thank GSRS Data Fusion Contest committee and Digital Globe for providing and making this dataset publicly available.

**Author Contributions:** All the authors listed contributed equally to the work presented in this paper.

**Conflicts of Interest:** The authors declare no conflict of interest.

## Abbreviations

The following abbreviations are used in this manuscript:

HRSI	High Resolution Satellite Imagery
LiDAR	Light Detection And Ranging
GCP	Ground Control Point
DSM	Digital Surface Model
SIFT	Scale Invariant Feature Transform
ISM	Image Shadow Mask
C-ISM	Cropped ISM
LSM	LiDAR Shadow Mask
PTLSM	Primary Transformed LiDAR Shadow Mask
CS-PTLSM	Cropped and Shifted PTLSM
STLSM	Secondary Transformed LiDAR Shadow Mask
GI	Geometric Index
RI	Radiometric Index
SF	Shadow Fitness
NCIFs	Normalized Color Invariant Features
DM	Displacements Map
ICEPM	Iterative Closest Edge Points Matching
ICP	Iterative Closest Points
PLS_Edges	Projected LiDAR and Shadows Edges
PAN_Edges	Panchromatic Edges
VCE	Variance Components Estimation

NrHOS	Number of the Homogeneous Observation Set
REVM	Relative Error Vectors Map
IbMF	Image based Matching Factor
LbMF	LiDAR based Matching Factor
AbMF	Average based Matching Factor

## References

1. Kumar, R.; Zhang, Y. A Review of optical imagery and airborne LiDAR data registration Methods. *Open Remote Sens. J.* **2012**, *5*, 54–63. [[CrossRef](#)]
2. Shorter, N.; Kasparis, T. Autonomous registration of LiDAR data to single aerial image. In Proceedings of the IEEE International Geoscience and Remote Sensing Symposium (IGARSS-2008), Boston, MA, USA, 7–11 July 2008; Volume 5, pp. 216–219.
3. Mastin, A.; Kepner, J.; Fisher, J. Automatic registration of LiDAR and optical images of urban scenes. In Proceedings of the IEEE Conference on Computer Vision and Pattern Recognition (CVPR-2009), Miami, FL, USA, 20–25 June 2009; pp. 2639–2446.
4. Parmehr, E.G.; Fraser, C.S.; Zhang, C.; Leach, J. Automatic registration of optical imagery with 3D LiDAR data using statistical similarity. *ISPRS J. Photogramm. Remote Sens.* **2014**, *88*, 28–40. [[CrossRef](#)]
5. Abedini, A.; Hahn, M.; Samadzadegan, F. An investigation into the registration of LiDAR intensity data and aerial images using the SIFT approach. In *The International Archives of the Photogrammetry, Remote Sensing and Spatial Information Sciences*; International Society of Photogrammetry and Remote Sensing: Beijing, China, 2008; Volume XXXVII, Part B1; pp. 169–175.
6. Ding, M.; Lyngbaek, K.; Zakhori, A. Automatic registration of aerial imagery with untextured 3DLiDAR Models. In Proceedings of the IEEE Conference on Computer Vision and Pattern Recognition (CVPR-2008), Anchorage, AK, USA, 23–28 June 2008; pp. 1–8.
7. Wang, L.; Neumann, U.; Fisher, J. A Robust approach for automatic registration of aerial images with untextured aerial LiDAR data. In Proceedings of the IEEE Conference on Computer Vision and Pattern Recognition (CVPR-2009), Miami, FL, USA, 20–25 June 2009; pp. 2623–2630.
8. Palenichka, R.M.; Zaremba, M.B. Automatic extraction of control points for the registration of optical satellite and LiDAR images. *IEEE Trans. Geosci. Remote Sens.* **2010**, *48*, 2864–2879. [[CrossRef](#)]
9. Toutin, T. Review Article: geometric processing of remote sensing images: Models, algorithms and methods. *Int. J. Remote Sens.* **2004**, *25*, 1893–1924. [[CrossRef](#)]
10. Sun, S.; Savalggio, C. Complex building roof detection and strict description from LiDAR data and orthorectified aerial imagery. In Proceedings of the 2012 IEEE International Geoscience and Remote Sensing Symposium, Munich, Germany, 22–27 July 2012; pp. 5466–5469.
11. Wong, A.; Orchard, J. Efficient FFT-accelerated approach to invariant optical-LiDAR registration. *IEEE Trans. Geosci. Remote Sens.* **2008**, *46*, 3917–3925. [[CrossRef](#)]
12. Kwak, T.S.; Kim, Y.; Yu, K.Y.; Lee, B.K. Registration of aerial imagery and aerial LiDAR data using centroids of plane roof surfaces as control information. *KSCE J. Civ. Eng.* **2006**, *10*, 365–370. [[CrossRef](#)]
13. Li, Y.; Gong, P.; Sasagawa, T. Integrated shadow removal based on photogrammetry and image analysis. *Int. J. Remote Sens.* **2005**, *26*, 3911–3929. [[CrossRef](#)]
14. Liu, J.; Tao, F.; Li, D. Shadow detection in remotely sensed images based on self-adaptive feature selection. *IEEE Trans. Geosci. Remote.* **2011**, *49*, 5092–5103.
15. Finlayson, G.D.; Hordley, S.D.; Lu, C.; Drew, M.S. On the removal of shadows from images. *IEEE Trans. Pattern Anal. Mach. Intell.* **2006**, *28*, 59–68. [[CrossRef](#)] [[PubMed](#)]
16. Sohn, H.G.; Yun, K.H. Shadow-effect correction in aerial color imagery. *Photogramm. Eng. Remote Sens.* **2008**, *74*, 611–618. [[CrossRef](#)]
17. Huang, J.; Xie, W.; Tang, L. Detection of and compensation for shadows in colored urban aerial images. In Proceedings of the 5th World Congress on Intelligent Control and Automation, Hangzhou, China, 15–19 June 2004; Volume 4, pp. 3098–3100.
18. Singh, K.K.; Pal, K.; Nigam, M.J. Shadow detection and removal from remote sensing images using NDI and morphological operators. *Int. J. Comput. Appl.* **2012**, *42*, 37–40.

19. Shao, Y.; Taff, G.N.; Walsh, S.J. Shadow detection and building-height estimation using IKONOS data. *Int. J. Remote Sens.* **2011**, *32*, 6929–6944. [[CrossRef](#)]
20. Comber, A.; Umezaki, M.; Zhou, R.; Ding, Y.; Li, Y.; Fu, H.; Jiang, H.; Tewkesbury, A. Using shadows in high resolution imagery to determine building height. *Remote Sens. Lett.* **2012**, *3*, 551–556. [[CrossRef](#)]
21. Thiel, K.H.; Cheng, F. Delimiting the building heights in a city from the shadow on a panchromatic SPOT-image. *Int. J. Remote Sens.* **1995**, *16*, 409–415.
22. Shettigara, V.K.; Sumerling, G.M. Height determination of extended objects using shadows in SPOT images. *Photogramm. Eng. Remote Sens.* **1998**, *64*, 35–44.
23. Maurer, T. How to pan-sharpen images using the gram-schmidt pan-sharpen method—A recipe. In *The International Archives of the Photogrammetry, Remote Sensing and Spatial Information Sciences*; International Society of Photogrammetry and Remote Sensing: Hannover, Germany, 2013; Volume XL-1/W1, pp. 239–244.
24. Morgan, M.F. Epipolar Resampling of Linear Array Scanner Scenes. Ph.D. Thesis, Department of Geomatics Engineering, University of Calgary, Calgary, AB, Canada, 2004.
25. Shahtahmassebi, A.; Yang, N.; Wang, K.; Moore, N.; Shen, Z. Review of shadow detection and de-shadowing methods in remote sensing. *Chin. Geogr. Sci.* **2013**, *23*, 403–420. [[CrossRef](#)]
26. Tasi, V.J.D. A comparative study on shadow compensation of color aerial images in invariant color models. *IEEE Trans. Geosci. Remote Sens.* **2006**, *44*, 1661–1671.
27. Barnard, K.; Finlayson, G. Shadow identification using color ratios. In Proceedings of the IS&T/SID Eighth Color Imaging Conference: Color Science, Systems and Applications, Scottsdale, AZ, USA, 7–10 November 2000; pp. 97–101.
28. Suny, A.H.; Mithila, N.H. A shadow detection and removal from a single image using lab color space. *IJCSI Int. J. Comput. Sci. Issues* **2013**, *10*, 270–273.
29. Finlayson, G.D.; Hordley, S.D. Color constancy at a pixel. *J. Opt. Soc. Am. A* **2001**, *18*, 253–264. [[CrossRef](#)]
30. Salvador, E.; Cavallaro, A.; Ebrahimi, T. Cast shadow segmentation using invariant color features. *Comput. Vis. Image Underst.* **2004**, *95*, 238–259. [[CrossRef](#)]
31. Gevers, T.; Smeulders, A.W.M. Color-based object recognition. *Pattern Recognit.* **1999**, *32*, 453–464. [[CrossRef](#)]
32. Safdarinezhad, A.; Mokhtarzade, M.; Valadan Zoej, M. Co-Registration of Satellite Images and Airborne LiDAR Data through the Automatic Bias Reduction of RPCs. *J. Sel. Top. Appl. Earth Obs. Remote Sens.* (under review).
33. Canny, J. A computational approach to edge detection. *IEEE Trans. Pattern Anal. Mach. Intell.* **1986**, *8*, 679–698. [[CrossRef](#)] [[PubMed](#)]
34. Reddy, B.S.; Chatterji, B.N. An FFT-based technique for translation, rotation, and scale-invariant image registration. *IEEE Trans. Image Process.* **1996**, *5*, 1266–1271. [[CrossRef](#)] [[PubMed](#)]
35. Kuglin, C.D.; Hines, D.C. The phase correlation image alignment method. In Proceedings of the IEEE Proceedings of Conference Cybernet and Society, New York, NY, USA, 1975; pp. 163–165.
36. Alba, A.; Aguilar-Ponce, R.M.; Viguera-Gómez, J.F.; Arce-Santana, E. Phase correlation based image alignment with subpixel accuracy. In Proceedings of the 11th Mexican International Conference on Artificial Intelligence, MICAI 2012, San Luis Potosí, Mexico, 27 October–4 November 2012; Advances in Artificial Intelligence. Volume 7629, pp. 171–182.
37. Besl, P.J.; McKay, H.D. A method for registration of 3-D shapes. *IEEE Trans. Pattern Anal. Mach. Intell.* **1992**, *14*, 239–256. [[CrossRef](#)]
38. Safdarinezhad, A.; Valadan Zoej, M.J. An optimized orbital parameters model for geometric correction of space images. *Adv. Space Res.* **2015**, *55*, 1328–1338. [[CrossRef](#)]
39. Amiri-Simkooei, A. Least-Squares Variance Component Estimation: Theory and GPS Applications. Ph.D. Thesis, Delft University of Technology, Delft, The Netherlands, 2007.

